Posted on 24 Nov 2022 — The copyright holder is the author/funder. All rights reserved. No reuse without permission. — https://doi.org/10.1002/essoar.10501011.1 — This a preprint and has not been peer reviewed. Data may be preliminary.

Can the GPS-data-based Global Ionospheric Maps provide relevant information on the polar ionospheric electron content distribution?

Manuel Hernández-Pajares[1], Haixia Lyu[1], Angela Aragon-Angel[2], Enric Monte[3], Jingbin Liu[4], jiachun an[5], and Hu Jiang[5]

[1]Universitat Politècnica de Catalunya
[2]Joint Research Centre
[3]Technical University of Catalonia
[4]Finnish Geospatial Research Institute
[5]Wuhan University

November 24, 2022

Abstract

The electron content distribution of the north and south polar ionosphere is analyzed from 2001 to the beginning of 2019 from the Global Ionospheric Maps of VTEC computed each 15 minutes by UPC-IonSAT with a tomographic-Kriging combined technique. We have found the VTEC footprint of features previously reported by different authors and with different techniques: tongues of ionization, trough and dawn-side drifting structure, flux transfer event, Theta-aurora VTEC observation at SP, and Storm enhanced density (SED) during major geomagnetic storms. Moreover, by means of an unsupervised clustering algorithm (Learning Vector Quantization), we have characterized the main features of the ionospheric electron content climatology, separately for the north and south poles. In particular a mean Tongue Of Ionization (TOI) behaviour over south polar ionosphere during 1345UT-1945UT, from November to February, i.e. in local spring and summer seasons, is confirmed in agreement with recent findings.

Can the GPS-data-based Global Ionospheric Maps provide relevant information on the polar ionospheric electron content distribution?

Manuel Hernández-Pajares[1,2], Haixia Lyu[1,2], Àngela Aragón-Àngel[3], Enric Monte-Moreno[4], Jingbin Liu[5,6,7], Jiachun An[8], Hu Jiang[8]

[1]UPC-IonSAT, Barcelona, Spain
[2]IEEC, Barcelona, Spain
[3]European Commission, Joint Research Centre (JRC), Directorate for Space, Security and Migration, Ispra, Italy
[4]UPC-TALP, Barcelona, Spain
[5]State Key Laboratory of Information Engineering in Surveying, Mapping and Remote Sensing, Wuhan University, Wuhan, China
[6]Collaborative Innovation Center of Geospatial Technology, Wuhan University, Wuhan, China
[7]Department of Remote Sensing and Photogrammetry and the Center of Excellence in Laser Scanning Research, Finnish Geospatial Research Institute, 02430 Masala, Finland
[8]Chinese Antarctic Center of Surveying and Mapping, Wuhan University, Wuhan, China

Key Points:

- The best-performing UPC GIMs (UQRG) have been analyzed over the poles during 1.5 Solar Cycles.
- The occurrence of several VTEC features is discussed and compared with previous works.
- The climatology of the main VTEC polar features is obtained in an unsupervised approach.

Corresponding author: Manuel Hernández-Pajares, `manuel.hernandez@upc.edu`

Abstract

The electron content distribution of the north and south polar ionosphere is analyzed from 2001 to the beginning of 2019 from the Global Ionospheric Maps of VTEC computed each 15 minutes by UPC-IonSAT with a tomographic-Kriging combined technique. We have found the VTEC footprint of features previously reported by different authors and with different techniques: tongues of ionization, trough and dawn-side drifting structure, flux transfer event, *Theta-aurora* VTEC observation at SP, and Storm enhanced density (SED) during major geomagnetic storms. Moreover, by means of an unsupervised clustering algorithm (Learning Vector Quantization), we have characterized the main features of the ionospheric electron content climatology, separately for the north and south poles. In particular a mean Tongue Of Ionization (TOI) behaviour over south polar ionosphere during 1345UT-1945UT, from November to February, i.e. in local spring and summer seasons, is confirmed in agreement with recent findings.

1 Introduction

This paper focuses on the characterization of relevant features of the polar ionospheric electron content distribution, in both North and South Polar hemispheres including polar caps (hereinafter NP and SP). This is achieved by using a new source of data, the Global Ionospheric Maps of Vertical Total Electron Content (VTEC) computed from Global Navigation Satellite Systems (GNSS) measurements, hereinafter GIMs, and during the most recent one and half solar cycles. First we justify the selection of GIMs that are probably the most accurate according to recent evaluations. Then we will analyze some polar ionospheric events, which had already been studied by other authors. Finally we will present the comprehensive results of unsupervised clustering of polar GIMs, showing the most frequent electronic content patterns, and the key occurrence characteristics. As main conclusion, we answer the following question in an affirmative way: Can the GIMs provide reliable information on the polar ionospheric electron content distribution, in spite of the reduced number of permanent receivers, and in spite of the limited spatial resolution, 5 deg in longitude and 2.5 deg in latitude (as it is pointed out for example in (Liu et al., 2014)).

In order to facilitate the understanding of the main techniques and context, three short introductions will be given in the next subsections on: (1) GIMs, (2) on one of the most discussed features of Polar ionosphere, and (3) on the Learning Vectorial Quantization (LVQ) unsupervised clustering algorithm.

1.1 The ionospheric data source: UQRG GIM and associated μ_2

The GIMs have been computed since 1998.5 in the context of the International GNSS Service (IGS). They have become a reliable and open source of ionospheric information, as it is shown in (Hernández-Pajares et al., 2011, 2009, 2017).

UPC-IonSAT is one of the, presently 7, IGS ionospheric analysis centers. It is computing the slightly most accurate GIMs on the global scale, identified as UQRG, as it can be seen in the long-term external assessment comparison with other GIMs of UPC and the GIMs of CODE, JPL, ESA, NRCAN, CAS and WHU, summarized in (Roma-Dollase et al., 2017). The UQRG performance, computed each 15 minutes with a latency of 1-2 days, is based on a combined tomographic estimation and kriging interpolation technique applied to 150-250 worldwide distributed GPS receivers.

The first step is the estimation of the mean electron density $(N_e)_{i,j,k}$ of the voxels providing a certain ionospheric partition $\{(i,j,k) : i = 1,\ldots,M_I, j = 1,\ldots,M_J, k = 1,\ldots,M_K\}$, which is 3D distributed (see Figure 1) in two layers from the ground-based

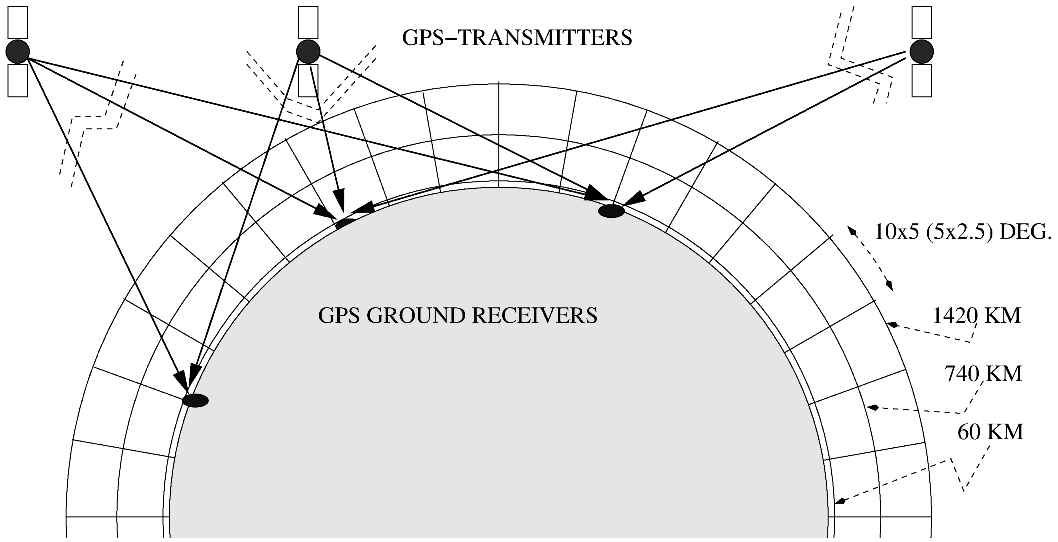

Figure 1. Simplified layout of the dual-layer voxel-based tomographic of the ionospheric electron content model, directly estimated from the actual dual-frequency GNSS carrier phase measurements only, by applying a Kalman filter.

dual-frequency GNSS carrier phase data only, the L_1 and L_2 in length units data, as:

$$L_I - (\lambda_1 - \lambda_2) \cdot \phi = \alpha \sum_{i=1}^{M_I} \sum_{j=1}^{M_J} \sum_{k=1}^{M_K} (N_e)_{i,j,k} \cdot \Delta l_{i,j,k} + B_I \tag{1}$$

where for each pair GNSS transmitter-receiver the ionospheric combination of carrier phases $L_I = L1 - L2$ is known (measured), and the wind-up correction due to the relative rotation of transmitter and receiver antenna is also known for permanent receivers (modelled), among the ray-path-length inside each illuminated voxel (i, j, k), $\Delta l_{i,j,k}$, which is computed by the very good approximation of straight-line propagation; finally $\alpha \simeq$ 1.05 m/TECU is the scaling factor derived from the Appleton-Hartree equations (see for instance (Hernández-Pajares et al., 2010) and (Hernández-Pajares et al., 2011)).

This model is solved by the TOMION-v1 software, developed by the first author, by implementing a forward Kalman filter which treats the mean electron densities as random walk processes in a Sun-fixed reference frame, and the ambiguities as random variables ("constants"). It significantly reduces the modelling error associated to the common fixed-height single-layer models, as it was demonstrated in (Hernández-Pajares et al., 1999), yielding more precise results because it avoids the usage of dual-frequency ionospheric pseudorange combination, strongly affected by the multipath and thermal noise.

The second step is the interpolation to fill the gaps of measurements, due to the lack of a full coverage of GNSS receivers, specially important over the oceans, South Hemisphere, Siberia and central Africa. This is done by taking as input interpolation data the individual VTEC values obtained from each measurement, after subtracting in previous equation the best estimation of the carrier phase ambiguity value. This is typically the last one of the continuous-phase transmitter-receiver arch. Afterward such Slant TEC is converted to VTEC with the single-layer mapping function with constant height at 450 km (see (Hernández-Pajares et al., 2011)), adopted in IGS by the different ionospheric computation centers. Finally the Kriging technique is applied on such individual VTEC estimations, which efficiently takes into account the ionospheric model decorrelation lengths in the interpolation process (Orús et al., 2005).

The GIM is not the only product we can obtain from this approach. Before the interpolation step, the fraction of topside electron content, μ_2 parameter, can be derived from the tomographic run. It is defined as follows from the two simultaneously estimated mean electron density values, $(N_e)_{i,j,1}$ and $(N_e)_{i,j,2}$ at mean heights of 450 km and 1130 km respectively (see Figure 1), and for the same horizontal voxel index (i, j):

$$(\mu_2)_{i,j} = \frac{(N_e)_{i,j,2}}{(N_e)_{i,j,1} + (N_e)_{i,j,2}} \tag{2}$$

μ_2 is obtained from the direct estimation in the tomographic model, and stored internally at UPC premises for all the daily global runs performed since 1998.5 within IGS. μ_2 is not only an indicator of the relative vertical distribution of free electrons as we will see below, but it is also a useful driver of an improved ionospheric mapping function at mid-latitudes, as it has been recently demonstrated in (Lyu et al., 2018).

1.2 Specific features of the polar ionosphere: TOI and polar cap patches

One special feature in the polar ionosphere is TOI, and associated patches. It is believed that they are plasma enhancements in the high latitude F region. Along their edges form steep electron density gradients, which can lead to degradation in HF radio communications and disturbance in satellite navigation and communication systems. Therefore, the study of the occurrence of TOI and polar cap patches is essential, which helps better understand the signature of the polar ionosphere. Despite the creditable efforts of many researchers ((Buchau et al., 1985),(Sojka et al., 1994), (Coley & Heelis, 1998),(Dandekar, 2002),(Noja et al., 2013),(David et al., 2016),(Liu et al., 2017),(Spicher et al., 2017),(Chartier et al., 2018)), the agreement has not been reached regarding the dependence factors of TOI or polar cap patches occurrence, partly because of data from diverse instruments, most of which (e.g. optical, HF and incoherent radar, and ionosonde) having limited spatial coverage or limited time span, or imperfect model simulation and partly due to different algorithms. Table 1 summaries the different results on polar cap patches dependence characteristics. For instance, using high-resolution TEC Maps from the Madrigal Database of Haystack Observatory, (David et al., 2016) found that north-hemisphere TOI or patches have Universal Time (UT) and seasonal dependence. However, whether polar patches are a seasonal or annual phenomenon is called into question by the finds of (Chartier et al., 2018). They used in-situ plasma density observations and topside TEC data to detect TOI and found that TOI is not only a winter phenomenon, but also occurs in Southern Hemisphere summer. In this paper, low-resolution VTEC Maps from ground-based GNSS stations are utilized for TOI and patches detection for the first time, which opens a new opportunity for detection and thus probably provides new evidence and arouses new insights for theoretical study, benefiting from longer time series of data.

1.3 The unsupervised clustering algorithm: Learning Vectorial Quantization

In order to better perform a first analysis of the large UQRG GIMs database, we have selected an unsupervised clustering system that enables us to find representative prototypes of the GIMs of the polar ionosphere. This will also allow to characterize its predominant morphology and features. Therefore we decided to use the LVQ as a clustering tool, (Kohonen, 2012) and (Murtagh & Hernández-Pajares, 1995). The reason for selecting the LVQ algorithm as opposed to other clustering algorithms, such as k-means and LBG (Linde et al., 1980), lies in the fact that it is an adaptive algorithm and that does need of any a-priori categorization which might bias the analysis, as it was shown for instance in classification of astronomical populations (Hernández-Pajares, 1993) or in GNSS ionospheric determination (Hernández-Pajares et al., 1997).

As it is detailed in (Hernandez-Pajares & Floris, 1994) the aim of this unsupervised classifier is to find a smaller set of $C = \{\mathbf{c}_1, \ldots, \mathbf{c}_p\}$ of p centroids that provides a good

Table 1. Main features of studies on polar patches and Tongues of Ionization.

Measurement source	Area	Dependence				Ref.
		Annual/ Seasonal	UT/ MLT(LT)	Geomag./ IMF	Solar Cycle	
Digisonde	NH	x	UT	x	Solar Cycle	(Buchau et al., 1985)
The Utah State University time dependent ionospheric model (TDIM) [a]	NH	Seasonal	UT	x	x	(Sojka et al., 1994)
The retarding potential analyzer(RPA), the ion drift meter(IDM), and the Langmuir probe aboard the DE 2 spacecraft	NH	Seasonal	UT	IMF	x	(Coley & Heelis, 1998)
foF2 data from Digital Ionospheric Sounding Systems at stations Sondrestromfjord and Qaanaaq	NH	Seasonal	MLT	IMF(weak)	Solar Cycle	(Dandekar, 2002)
9-years CHAMP TEC data	NH, SH	Annual	MLT	IMF	Solar Cycle	(Noja et al., 2013)
Madrigal GPS TEC Maps (high-resolution)	NH	Seasonal	UT	x	x	(David et al., 2016)
The National Center for Atmospheric Research Thermosphere-Ionosphere Electrodynamics General Circulation Model (TIEGCM)	NH, SH Hemispheric asymmetry of TOI intensity	Seasonal dependence of UT effects on TOI intensity	UT	IMF	x	(Liu et al., 2017)
Swarm: in situ plasma density measurements	NH, SH	Seasonal	x	IMP	x	(Spicher et al., 2017)
Swarm: in situ electron dens. by Langmuir probe and TEC from POD GPS receiver	NH, SH	Annual	x	Kp-independent	x	(Chartier et al., 2018)

[a] Switch between the A and DE patterns every 30 min with constant inputs: (a) The auroral oval parameters, specifically the electron energy flux and average energy, were obtained from (Hardy et al., 1987) model. (b) A solar maximum condition was assumed, represented by an F10.7 index of 210.

approximation of the original set S of n ionization-level-independent, i.e. normalized polar GIMs (input space) with m attributes, encoded as vectors $\mathbf{x} \in S$. Intuitively, this should mean that for each $\mathbf{x} \in S$ the distance $\|\mathbf{x} - \mathbf{c}_{f(x)}\|$ between x and the closest centroid $\mathbf{c}_{f(x)}$ should be small.

The LVQ clustering algorithm can be summarized as follows:

1. We define the number of centroids p and the number of times (number of epochs) that the whole database is passed through the algorithm.
2. We initialize the values $C = \{\mathbf{c}_1, \ldots, \mathbf{c}_p\}$ of the p centroids from p input observations randomly selected: $C = \{\mathbf{c}_1, \ldots, \mathbf{c}_p\}$. After training, every centroid $l \in \{1, \ldots p\}$ will represent a set of normalized polar GIMs, and the weight vector $\mathbf{c}_l$ will approximate to the *center of mass* of this set.
3. We initialize the update counter: i
4. For iteration 1 to number of epochs:

   (a) For each of the n training vectors of the overall data base, $\mathbf{x}_i$, the following procedures are carried out:

      i. We find the node k whose weight $\mathbf{c}_k$ best approaches $\mathbf{x}_i$ (d represents in our case the Euclidean distance in the space $\mathbf{R}^n$, where n is the number of grid values of any polar GIM: $d(\mathbf{c}_k, \mathbf{x}_i) \leq d(\mathbf{c}_l, \mathbf{x}_i)$, $\forall l \in \{1, \ldots, p\}$.

      ii. We update the weight of the winning node k and its neighbours, $N_k(i)$, approaching the training vector as closely as possible:

$$\mathbf{c}_l(i) = \begin{cases} \mathbf{c}_l(i-1) + \alpha(i)\,[\mathbf{x}_i - \mathbf{c}_l(i-1)] & \forall l \in N_k(i) \\ \mathbf{c}_l(i-1) & \forall l \in \{1, \ldots, p\} - N_k(i) \end{cases} \tag{3}$$

   Here $\alpha(i)$ is a suitable, monotonically decreasing sequence of scalar-valued gain coefficients, $0 < \alpha(i) < 1$. The justification of this parameter is related to the Robbins-Monro algorithm (Robbins & Monro, 1951), which guarantees the convergence an iterative estimation of a mean parameter of a Gaussian distribution. A choice that guarantees a fast convergence is, for example, a linear decrease of $\alpha(i)$ during the first 1000 epochs in a range between 0.9 and 0.1 (ordering period). Then after this initial phase, $\alpha(i)$ should attain a final value below or equal 0.01, with a decrease proportional to the inverse of the iteration number, i.e. $\alpha(i) \propto 1/i$.

The final point density function of $\{\mathbf{c}_1, \ldots, \mathbf{c}_p\}$ is an approximation of the continuous probability density function of the vectorial input variable $\mathbf{g}(\mathbf{x})$ (actually if follows $[\mathbf{g}(\mathbf{x})]^{\frac{m}{m+2}}$, (Kohonen, 1990), p. 1466).

2 GIM detection examples of reported polar ionospheric features

In this section we confirm the detection of specific polar ionospheric features, reported by different authors, within the GIM VTEC: tongue of ionization, ionospheric trough, storm enhanced density, flux transfer event, and theta-aurora.

2.1 Tongue of Ionization

The GIM VTEC map corresponding to the NP TOI reported in (David et al., 2016), at 1700UT on 5 November 2012 is shown at the left-hand plot of Figure 2. This is fully consistent in extension, shape and VTEC level (up to around 20 TECU in the TOI) with Figure 2 of (David et al., 2016), obtained with a higher resolution VTEC mapping technique. In addition, a simultaneous TOI happened in the SP, which can be seen at the right-hand plot of Figure 2.

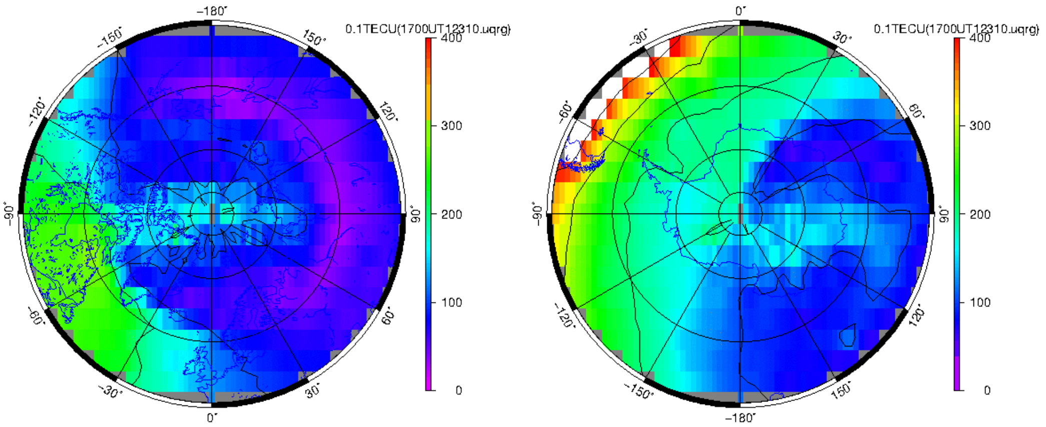

Figure 2. VTEC maps at NP (left) and SP (right) during 5 November 2012 at 1700UT. The VTEC scale in given in 0.1 TECUs, the same as the remaining VTEC GIMs in this section.

Another interesting feature about TOIs in the SP is that most of the TOIs cross or direct to the South Magnetic Pole (see four examples at different UT times in Figure 3), which is located in the range (E136-E138,S63-S64) deg from 1998 to 2015. The frequent appearance of this feature shows the TOI bends from its origin at the daylight hemisphere side towards the magnetic pole. It is noticeable that the μ_2 values within the TOIs are typically lower than those in the surrounding night polar ionosphere, which implies the associated electron content being distributed significantly lower in height. While, when TOI and the daylight areas are compared, the μ_2 values change slightly. It indicates that the ionospheric effective height, where the free electron can be considered concentrated in a simplified view, almost keeps constant in the TOI from the day-side part. This agrees with the result that the virtual heights in the ionograms did not change during transit of the arcs through the zenith found in (Buchau et al., 1983).

2.2 Trough and dawn-side drifting structure

In the left panel of Figure 4, it is easy to see a region of depleted ionization (in purple), i.e. trough, where μ_2 values above 0.8 (corresponding to the represented values of $\mu_2{+}1 > 1.8$) are greater than those in the surrounding area. Big μ_2 implying high ionospheric effective height, probably corresponds to a typical trough feature - enhanced electron temperature. According to the proportional relationship between temperature and scale height, the high temperature would increase the scale height in the topside part, resulting in slow decay of electron density above the peak, thus increasing the ionospheric effective height. Apart from the trough, enhanced ionization area in the polar cap in a shape of circle can be seen in the unsupervised cluster representatives below. In this case, at 1745 UT, the interplanetary magnetic field (IMF) y-component, B_y, is negative and the z-component, B_z, is switching from northward to southward (see Figure 5). The convection theory (Sojka et al., 1993) suggests that, for negative B_y when IMF is southward, the flow is across the dusk-side of the polar cap. While the structure in the VTEC map appears to be dawn-side, thus the convection pattern needs to be further investigated by theoretical model.

2.3 Storm enhanced density

During geomagnetic storms, F-region ionospheric plasma from lower latitudes in the afternoon sector is transported polewards. Consequently, a latitudinally narrow region of SED and increased TEC is carried toward higher latitudes in the noon sector (Foster,

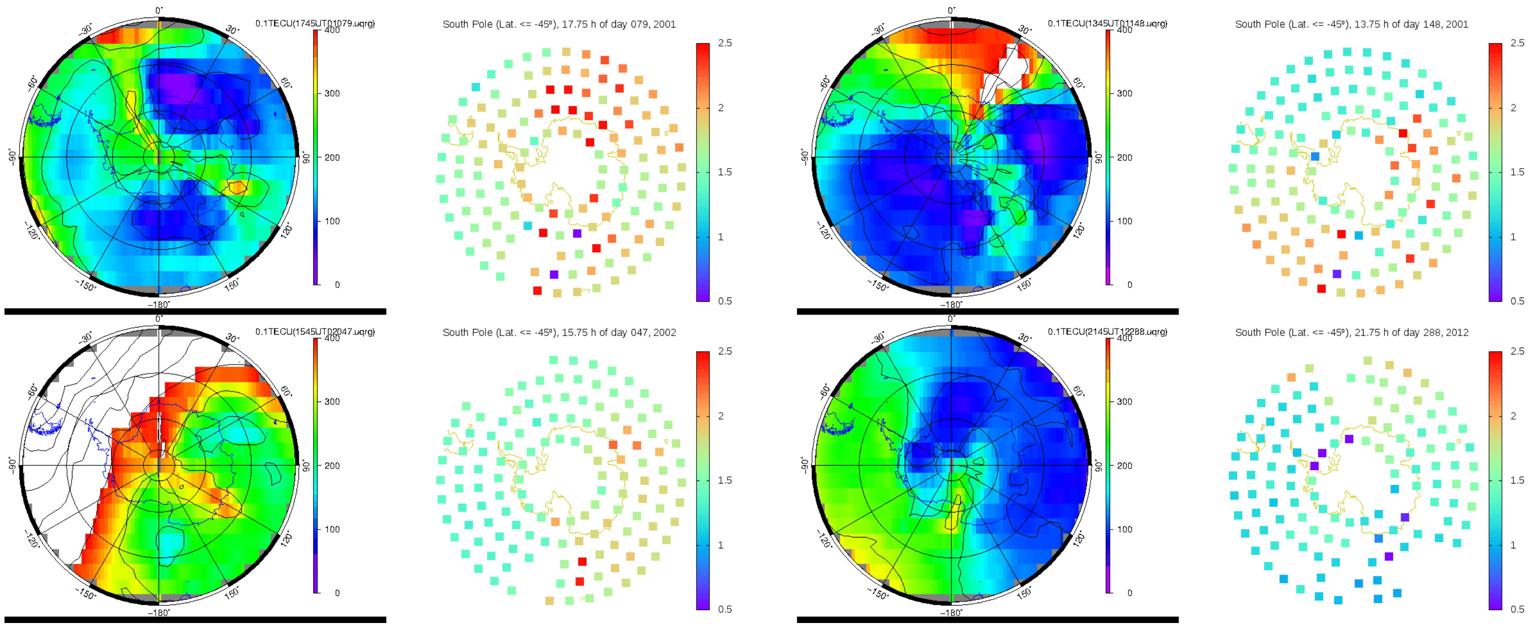

Figure 3. Four typical VTEC polar GIMs at SP showing TOIs, and the associated μ_2 distribution, corresponding to the year-DOY-UT: 2001-079-1745, 2001-148-1345, 2002-047-1545 and 2012-288-2145 (from left to right, from top to bottom). The white area in all the VTEC maps of this context represents VTEC values greater than 40 TECU. In the right panel of each subplot, the values in colorbar are μ_2+1

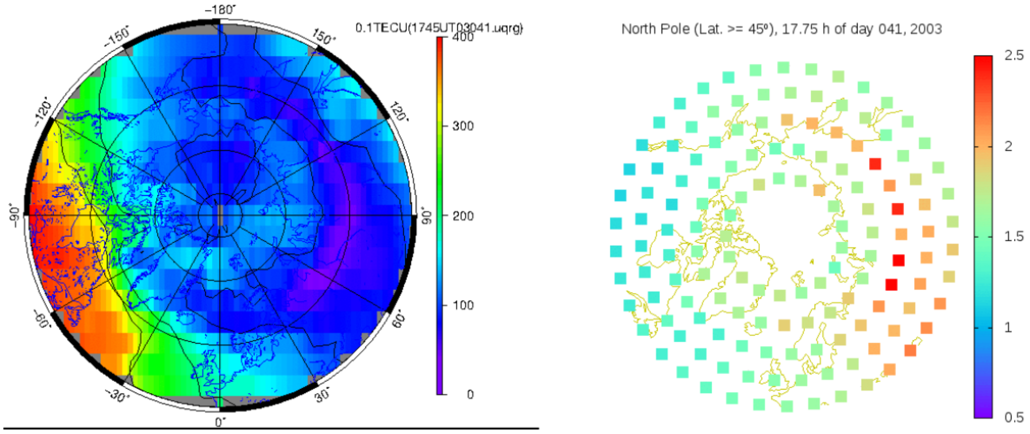

Figure 4. VTEC and μ_2 maps in northern hemisphere at 1745 UT on DOY 041, 2003 from UQRG GIMs. In the right panel, the values in colorbar are μ_2+1.

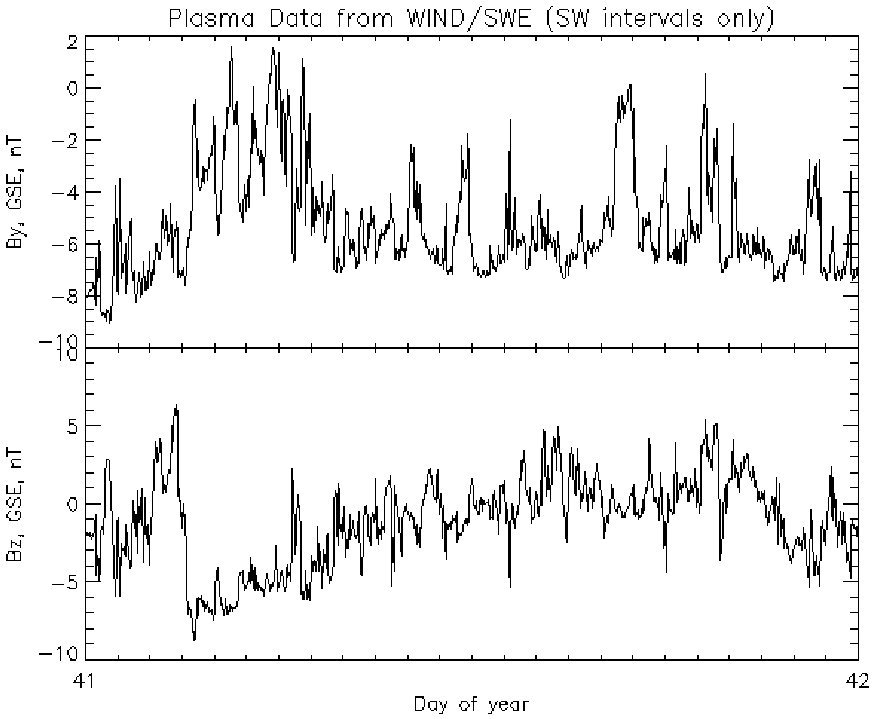

Figure 5. IMF B_y and B_z components on DOY 041, 2003, downloaded from https://omniweb.gsfc.nasa.gov/ftpbrowser/wind_swe_2m.html

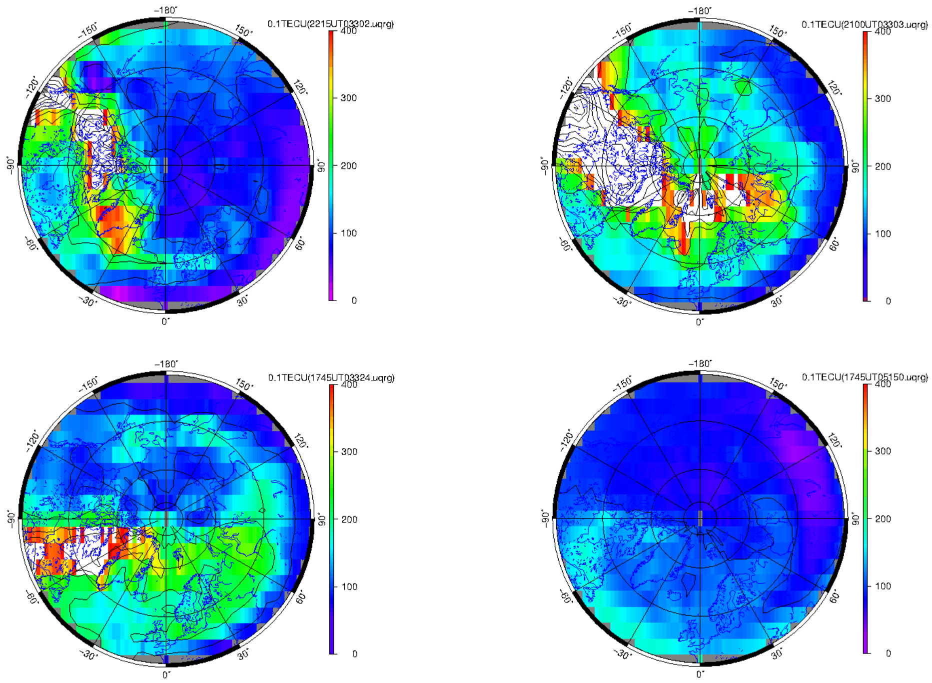

Figure 6. Four cases in NP for storm enhanced TEC on two days (DOY 302 2215UT and 303 2100UT, 2003) of "Halloween Storms" (top), on DOY 324 1745UT, 2003 (bottom-left), and DOY 150 1745UT, 2005 (bottom-right), directly obtained from the corresponding UQRG GIMs.

1993). The distribution of VTEC in the northern hemisphere during major geomagnetic storms, including Halloween Storms of 2003 and the other two cases with Kp index around 7 and 8.7 respectively, are shown in Figure 6. The feature that the enhanced TEC plumes are concentrated in the pre-midnight and postnoon sector (Foster et al., 2005) can be seen in these four examples on Halloween Storms of 2003, DOY 324, 2003, and DOY 150, 2005.

2.4 Flux transfer event (FTE)

On 13 February 2001, the transpolar propagation of large-scale Traveling Ionospheric Disturbances (TIDs) from the nightside source region to the dayside is reported by (Cai et al., 2011). On 14 February, the magnetospheric flux transfer events are observed by Cluster spacecraft (Wild et al., 2001, 2003). The VTEC maps in both hemispheres (see Figures 7 and 8) show the ionospheric response to these events. Ionospheric VTEC Maps in the NP from 11 February (DOY 041) to 17 February (DOY 047) 2001 have been closely examined. It is worth mentioning that only a series of VTEC maps from 1900 UT of DOY O44 to 0500 UT of DOY 045 with 2-hour interval has been shown in figures to avoid excessive length. TOI occurred and lasted for around 4 and 5 hours after 1500 UT for DOY 041 and 042 respectively. From 2330 UT of DOY 043 to 0100 UT of DOY 044, two-TOI-like structure presented, which is similar to that in the bottom-left plot of Figure 7. Afterwards, between 1700 UT of DOY 044 and 0200 UT of DOY 045, very strong TOI appeared, then drifting to the duskside and back to the dawnside later, and gradually forming a loop and then separating into two-TOI-like structure again. In the second half day of DOY 045, TOI was formed from 1315 UT to 1730 UT. Whereas, on both DOY 046 and 047, no obvious TOI showed up. From VTEC maps in the SP, TOI appeared in two time slots [0600 UT, 0730 UT] and [2145 UT, 2330 UT] on DOY 044, 2001, three days

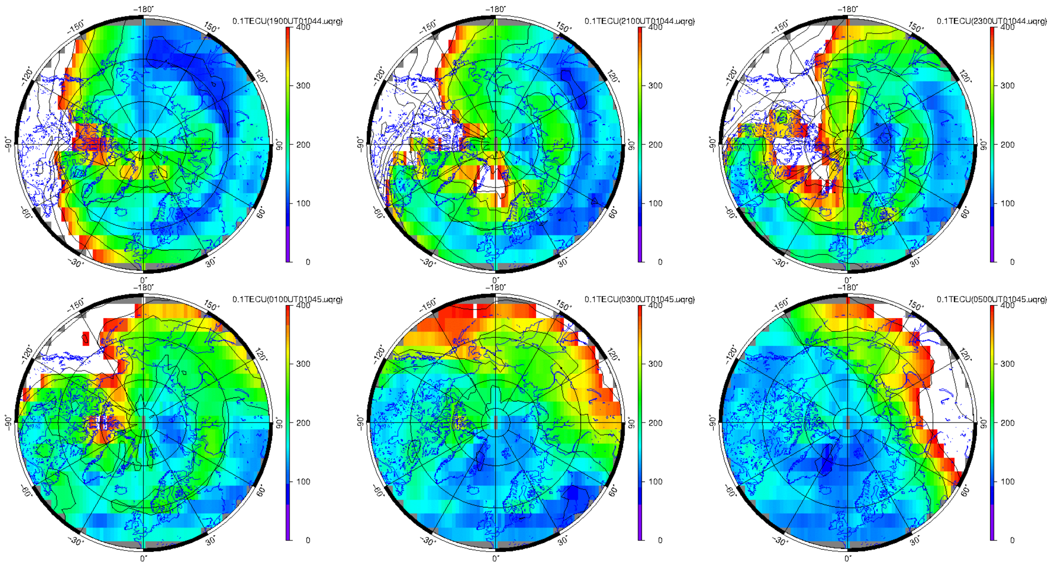

Figure 7. From left to right and from top to bottom: VTEC maps from UQRG GIMs, showing the development of TOI and patches each 2 hours from 13 February 1900UT to 14 February 0500UT, 2001 in the NP.

before which no TOI showed up. What is interesting is a swan-shape structure, which is drifted TOI, occurred around 0200 UT on DOY 045, 2001. And on the same day, TOI can also be seen from 1130 UT to 1500 UT. The specific feature in the NP that two-TOI-like structure appeared and merged later on might be related to FTE or directly to the geomagnetic disturbance caused by FTE. The mechanism is still unknown and it is worth investigating with other measurements.

2.5 *Theta-aurora* VTEC observation at SP

During 1638-2000UT of September 15, day 258 of year 2005, direct observations of closed magnetic flux, in correspondence with a small and thin transpolar arc over SP, were taken by the FUV Wideband Imaging Camera of the IMAGE satellite (see Figure 4A in (Fear et al., 2014)). We have detected the formation of a sort of transpolar arc, longer and thicker, during this day, before the pass of the satellite. It can indeed be seen in Figure 9, in the SP VTEC snapshots at 1130UT and 1530UT, with two associated depletions at both sides. Moreover, a ring of enhanced electron content formed, very clear at 1930UT, and was located around the South Magnetic pole, about (E138,S64) deg at such a time, with a radius of 15 deg approximately. The forementioned features together with a mid transpolar arc that can be considered as part of such "theta-aurora" happened during Northward IMF as explained in (Fear et al., 2014).

3 Looking for predominant features in the polar ionosphere: Unsupervised clustering of the Polar GIMs

We analyzed the time series from January 1st, 2001 to February 14, 2019, which consisted of about 640000 UQRG GIMs, sampled at time intervals of 15 minutes, separately for each UT. The analysis was done in geographic coordinates but independently for each daily UT, similarly to (David et al., 2016), as a simple way of analyzing directly the values provided by the GIM, and previously by mu2, avoiding any interpolation, and with very slow time-varying magnetic coordinates for each grid point due to the long-

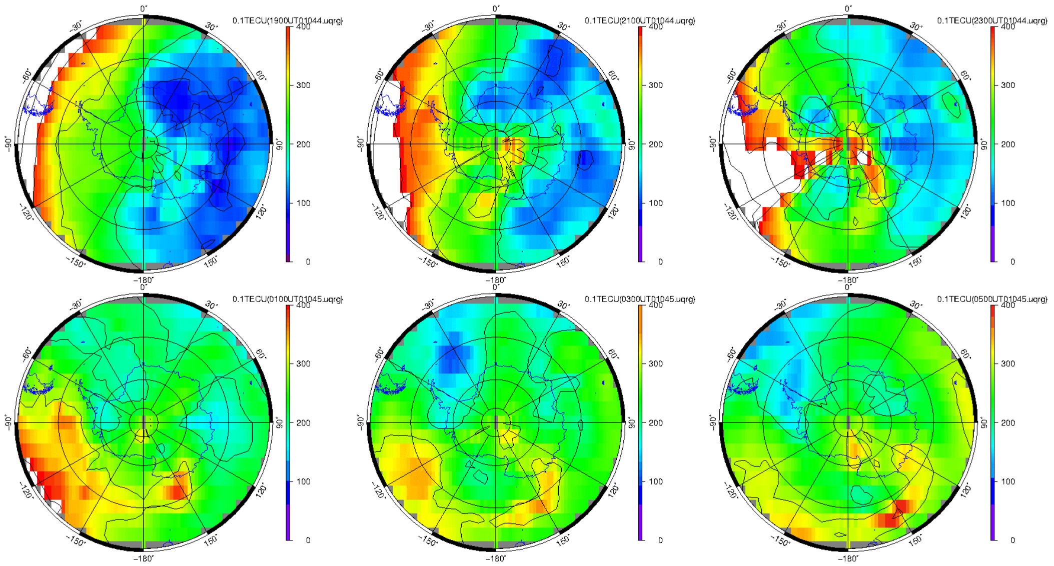

Figure 8. From left to right and from top to bottom: VTEC maps from UQRG GIMs, showing the development of TOI and patches each 2 hours from 13 February 1900UT to 14 February 0500UT, 2001 in the SP.

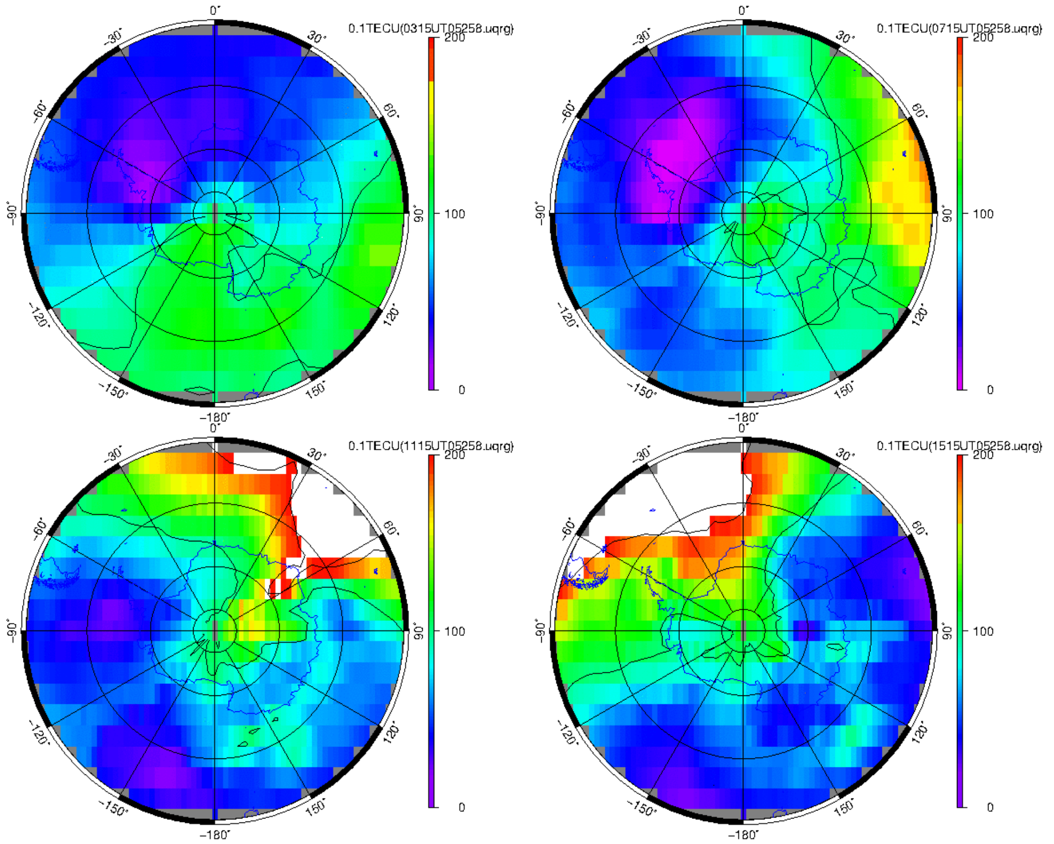

Figure 9. SP VTEC during 15 September, day 258, of year 2005 at 0715UT, 1115UT (first row), 1515UT and 1915UT (second row), extracted from UQRG GIM.

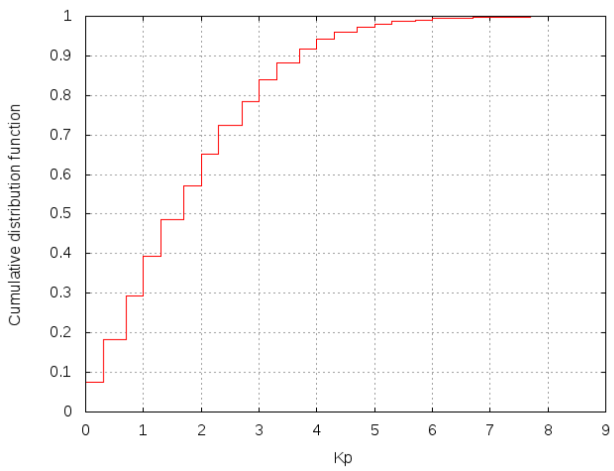

Figure 10. Kp cumulative probability distribution function from 2001.0 to 2018.3 (source: NOAA).

term drift of the magnetic poles. The NP and SP were split with N45 deg and S45 deg as the respective borders, and maintaining the GIM resolution of 5 deg, 2.5 deg and 15 minutes in longitude, latitude and time, high enough to detect large-scale patches with hundreds of kilometers to several thousand kilometers in the horizontal dimension. To study this long time period we dispose of more than 1,260,000 polar GIMs to be used in the cluster procedure after normalizing each polar GIM with with the standard L2 norm. In this way we show be able to: (1) detect the most frequent features, also with low ionization level, e.g. in night-time during minimum solar cycle conditions; and (2) to use the inner product among the normalized vectors representing each polar GIM to derive their distance. This was done independently for each UT, by means of the unsupervised LVQ algorithm as was indicated in the introduction. The use of the LVQ allowed us to detect the climatology for different local time and magnetic field conditions.

The study was started with up to $3x3 = 9$ potential centroids, and the clusters obtained presented subtle differences not suitable for a first comprehensive study, compared with the more clear differences, easier to interpret, when up to $2x2 = 4$ potential centroids are searched. And the typical clustering result of three centroids obtained in the majority of the 96 UT values (from 0000UT, each 15 minutes) can be interpreted like the existence of three typical groups of GIMs, which are interpreted below. Additionally, we have considered the polar maps of the topside electron content fraction, μ_2, which has been helpful to interpret the vertical distribution in some cases. The geomagnetic activity has not been taken into account due to the relatively small percentage of significantly active days, at it can be seen in the cumulative probability distribution function of Kp since 2001.0 to 2018.3 represented in Figure 10, where at least the 92% of the time is free from geomagnetic storms (Kp< 4).

The unsupervised clustering of the normalized North Polar GIMs defined above N45 deg hours from 0145UT can be seen in the Appendix every 2 hours in Figure A1, Figure A4, Figure A7, and Figure A10. In order to detect solar-cycle-related patterns, the corresponding histograms of occurrence per year are represented in Figure A2, Figure A5, Figure A8 and Figure A11. Apart from that, the occurrence per day of year, to detect seasonal patterns, is included in Figure A3, Figure A6, Figure A9 and Figure A12. A typical ring of relatively high electron content is shown, specially from 2345UT to 1545UT (third row of plots), under Solar Mininum conditions and from November to February, i.e. within local fall and winter seasons. A less clear ring is also found during Solar Maximum conditions in a similar UT time interval but mostly during the period from September to November and February to March (second row of plots). Mean relative structures of electron content resembling TOIs or partial rings can be also found during the time from 1745UT to 2145UT in both conditions, i.e. in corresponding rows 3 and 2 of plots as well as in the 4th row of plots, when it is populated in the unsupervised clustering computation. Finally, the predominant cluster of relative polar NP VTEC (first row of clusters) presents a flatter shape concentrated in local spring and summer seasons.

Similarly to the NP, the unsupervised clustering of the normalized South Polar GIMs, defined below S45 deg, can be seen since every 2 hours from 0145UT in Figure A13, Figure A16, Figure A19, and Figure A22. And the corresponding histograms of occurrence per year are represented in Figure A14, Figure A17, Figure A20 and Figure A23 for detecting solar-cycle related patterns. Moreover, the occurrence per day of year, to detect seasonal patterns, is included in Figure A15, Figure A18, Figure A21 and Figure A24. The polar GIM centroids at SP show a typical relative bimodal electron content depletion, specially from 2145UT to 0545UT (third row of plots), more frequent at Solar Minimum conditions and from April to August, i.e. within local fall and winter seasons. A predominant single depletion is also found more frequently during Solar Maximum conditions in a similar UT time interval but mostly during March-April and July-October (second row of plots). Other structures appear during the rest of UTs, 0745UT to 1945UT, for the same seasons and predominant Solar Cycle phases in third and second rows of centroids: relative theta-aurora-like pattern in 1145UT-1575UT (see corresponding example in previous section) and curly electron content shapes (third row), and TOIs (second row), with similar yearly and seasonal occurrence as in 0745UT-1945UT interval, i.e. Solar Maximum conditions during March-April and July-October. The first row of SP centroids show a flatter distribution as well, but with a clear mean TOI behaviour during 1345UT-1945UT, from November to February, i.e. in local spring and summer seasons, in agreement with (Chartier et al., 2018).

4 A very first insight on the accuracy of real-time polar GIMs

In order to provide a first insight on the potential feasibility of polar VTEC monitoring in real time (RT), the assessment of four different GIMs, two in RT (NOWG and URTG), one rapid (UQRG) and one under final latencies (IGSG), has been done vs +50,000 JASON3 VTEC measurements. We have followed one of the two GIM assessment methodologies recommended in (Hernández-Pajares et al., 2017). The analysis has been extended to the five available days in 2018 with complete data from most of the GIMs. The summaries can be seen in Table 2 for JASON3 measurements over the ocean at NP with latitudes above 50 deg, and in Table 3 for measurements with latitudes below -50 deg. If we focus on the Standard Deviation of the JASON3 minus GIM VTEC as a performance figure, free from the bias of the altimeter (see for instance(Roma-Dollase et al., 2017)), it is evident the suitability of rapid UQRG with typical latency of one day, with performances similar (slightly better at NP and slightly worse at SP) than the final IGS-combined-one (IGSG, see a recent assessment in (Roma-Dollase et al., 2017)) with latency of two weeks. Nevertheless, the RT-GIM NOWG is not performing apparently so well, but the RT-GIM URTG, during the available day with complete data and normal functioning (2018 360) is performing closer to both rapid-UQRG and final-IGSG GIMs. The visual comparison of the four GIMs during 0400UT, 1200UT and 2000UT during the day with full availability of the four GIMs, in both NP (Figure 11) and SP (Figure 12), show higher agreement between the GIMs presenting smaller errors, e.g. standard deviation regarding to JASON3 VTEC, consistently with this assessment over the polar seas.

Table 2. NP GIMs assessment based on the VTEC[JASON3]-VTEC[GIM] statistics for latitude ≥50 deg. The compared GIMs are those with RT- (NOWG from IPS, URTG from UPC-IonSAT excepting when the full functioning [*] or prediction [**] were not activated), rapid- (UQRG from UPC-IonSAT) and final- (IGSG, the final combined IGS GIM) latencies during five days in 2018 with complete data of NOWG, UQRG and IGSG.

DOY 2018	VTEC[JASON3]-VTEC[GIM] / TECUs Std.Dev.				Bias				VTEC [JASON3] Bias	# JASON3 Meas.
	NOWG	URTG	UQRG	IGSG	NOWG	URTG	UQRG	IGSG		
282	2.6	[*]	1.6	1.7	-2.8	[*]	-0.8	-1.1	3.8	3225
293	3.1	[*]	1.8	2.1	-0.1	[*]	-0.9	-0.9	5.5	2686
329	5.1	[**]	1.7	1.8	-3.7	[**]	-1.2	-0.3	4.3	3070
336	4.7	[**]	1.5	1.8	-3.1	[**]	-1.7	-1.2	4.0	3084
360	3.7	2.4	1.7	1.7	-3.9	-1.3	-0.8	-0.1	2.3	2707

Table 3. SP GIMs assessment based on the VTEC[JASON3]-VTEC[GIM] statistics for latitude ≤-50 deg. The compared GIMs are those with RT- (NOWG from IPS, URTG from UPC-IonSAT excepting when the full functioning [*] or prediction [**] were not activated), rapid- (UQRG from UPC-IonSAT) and final- (IGSG, the final combined IGS GIM) latencies during five days in 2018 with complete data of NOWG, UQRG and IGSG.

DOY 2018	VTEC[JASON3]-VTEC[GIM] / TECUs Std.Dev.				Bias				VTEC [JASON3] Bias	# JASON3 Meas.
	NOWG	URTG	UQRG	IGSG	NOWG	URTG	UQRG	IGSG		
282	2.6	[*]	2.3	2.1	1.6	[*]	-1.0	-0.7	5.7	7075
293	2.7	[*]	2.3	2.0	1.6	[*]	-1.8	-1.1	4.5	7521
329	3.5	[**]	2.1	1.9	5.3	[**]	-2.7	-1.6	7.9	7760
336	3.2	[**]	2.8	2.3	5.5	[**]	-3.3	-0.7	8.4	9221
360	3.3	3.3	1.9	2.0	5.1	-0.8	-2.8	-1.6	8.7	11551

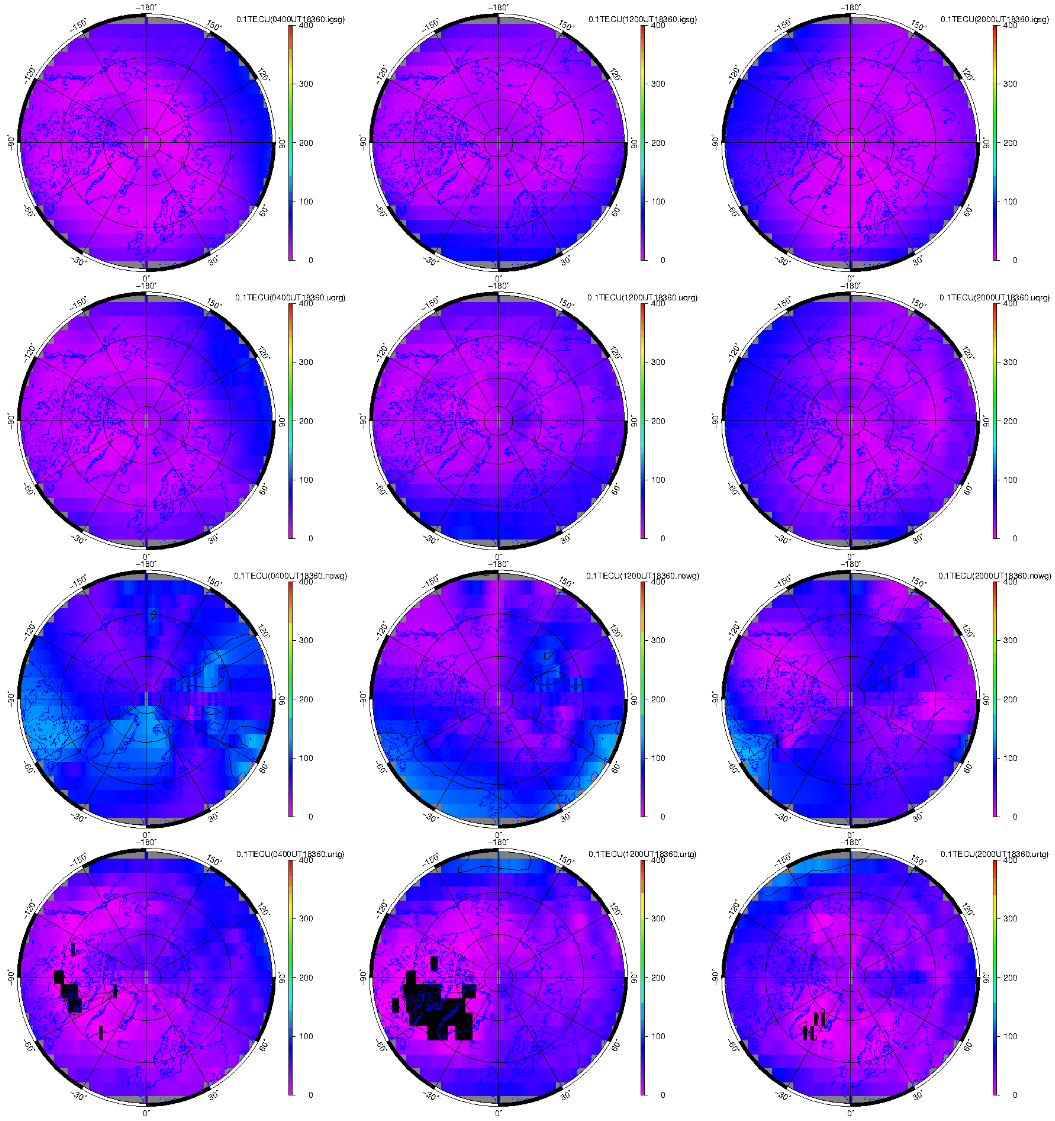

Figure 11. VTEC comparison from NP final- (IGSG from IGS combination in first row), rapid- (UQRG from UPC-IonSAT in second row) and RT-GIMs (NOWG from IPS and URTG from UPC-IonSAT in third and fourth rows), for 0400UT, 1200UT and 2000UT of day 360 of year 2018.

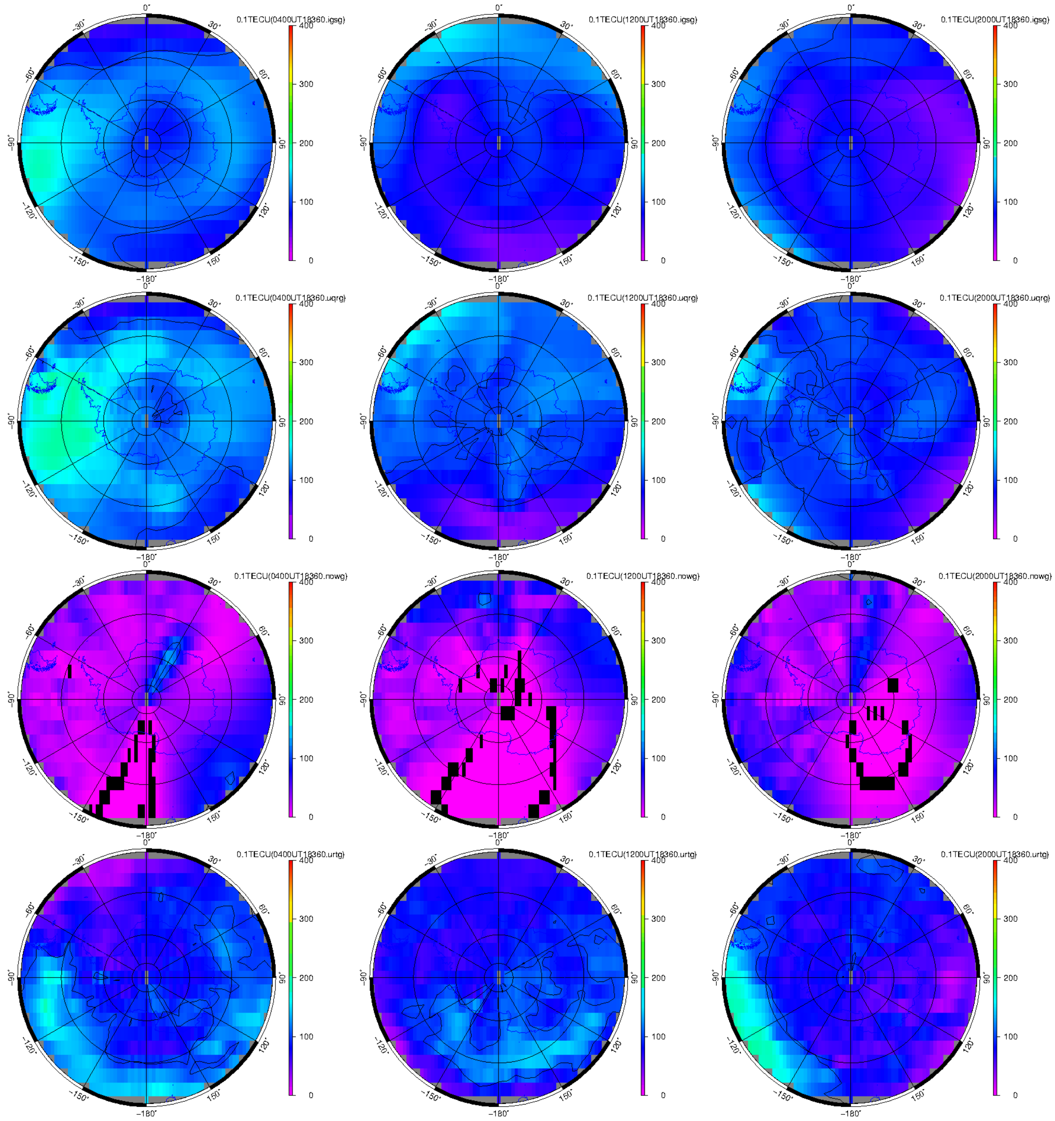

Figure 12. VTEC comparison from SP final- (IGSG from IGS combination in first row), rapid- (UQRG from UPC-IonSAT in second row) and RT-GIMs (NOWG from IPS and URTG from UPC-IonSAT in third and fourth rows), for 0400UT, 1200UT and 2000UT of day 360 of year 2018.

5 Conclusions

In this work we have shown that the Global Ionospheric Maps, computed by UPC-IonSAT since 1998 as IGS ionospheric analysis center, are able to provide VTEC footprint of different phenomena of polar ionosphere. Namely, we have shown examples of Tongues of Ionization, trough and dawn-side drifting structure, flux transfer event, *Theta-aurora* VTEC observation at SP, and storm enhanced density during major geomagnetic storms. All of them are in agreement with the results reported by other authors, with different techniques and sources of measurements. Some of these phenomena are supported as well by the topside electron content fraction, simultaneously estimated by UPC-IonSAT in the tomographic computation process of the GIMs. Moreover, thanks to the unsupervised clustering provided by the LVQ neural network of the normalized VTEC maps, it has been characterized the seasonal, annual, solar-cycle, UT dependence in North and South pole occurrences of TOIs, electron content rings, transpolar arcs (theta-aurora) and bimodal depletions. Finally, the finding that for the south hemisphere polar region most TOI activity occurs in local summer has been confirmed.

We consider this work can help to promote the usage and further analysis of the huge amount of information on polar ionosphere contained in the Global Ionospheric Maps, computed from the nineties by some analysis centers.

Acknowledgments

The data for this work are available and can be requested from the authors, in particular from Manuel Hernndez-Pajares (manuel.hernandez@upc.edu). This work has been supported by the POLarGIMs project funded by European Commission Joint Research Centre (JRC). We thank the National Space Science Data Center (NSSDC), Space Physics Data Facility (SPDF) and Principal Investigator K.W. Ogilvie at GSFC, A.J. Lazarus at MIT and A. Aran at *Universitat de Barcelona* (UB), for the access of IMF data. The first author is very thankful as well with Pere Ramos, who preserved a copy of the LVQ source code used in the above mentioned former astronomical studies.

References

Buchau, J., Reinisch, B., Weber, E., & Moore, J. (1983). Structure and dynamics of the winter polar cap f region. *Radio Science*, *18*(6), 995–1010.

Buchau, J., Weber, E., Anderson, D., Carlson Jr, H., Moore, J., Reinisch, B., & Livingston, R. (1985). Ionospheric structures in the polar cap: Their origin and relation to 250-mhz scintillation. *Radio Science*, *20*(3), 325–338.

Cai, H. T., Yin, F., Ma, S. Y., & McCrea, I. W. (2011). Observations of agw/tid propagation across the polar cap: a case study. In *Annales geophysicae* (Vol. 29).

Chartier, A. T., Mitchell, C. N., & Miller, E. S. (2018). Annual occurrence rates of ionospheric polar cap patches observed using swarm. *Journal of Geophysical Research: Space Physics*, *123*(3), 2327–2335.

Coley, W. R., & Heelis, R. A. (1998). Structure and occurrence of polar ionization patches. *Journal of Geophysical Research: Space Physics*, *103*(2), 2201–2208.

Dandekar, B. (2002). Solar cycle dependence of polar cap patch activity. *Radio Science*, *37*(1), 1-13.

David, M., Sojka, J., Schunk, R., & Coster, A. (2016). Polar cap patches and the tongue of ionization: A survey of gps tec maps from 2009 to 2015. *Geophysical Research Letters*, *43*(6), 2422–2428.

Fear, R. C., Milan, S. E., Maggiolo, R., Fazakerley, A. N., Dandouras, I., & Mende, S. B. (2014). Direct observation of closed magnetic flux trapped in the high-latitude magnetosphere. *Science*, *346*(6216), 1506–1510.

Foster, J. C. (1993). Storm time plasma transport at middle and high latitudes.

Journal of Geophysical Research: Space Physics, *98*(A2), 1675–1689.
Foster, J. C., Coster, A. J., Erickson, P. J., Holt, J. M., Lind, F. D., Rideout, W., ... Rich, F. J. (2005). Multiradar observations of the polar tongue of ionization. *Journal of Geophysical Research: Space Physics*, *110*(A9).
Hardy, D. A., Gussenhoven, M. S., Raistrick, R., & McNeil, W. J. (1987). Statistical and functional representations of the pattern of auroral energy flux, number flux, and conductivity. *Journal of Geophysical Research: Space Physics*, *92*(A11), 12275–12294.
Hernández-Pajares, M. (1993). Can a local bulge be differentiated? *Monthly Notices of the Royal Astronomical Society*, *264*(1), 1–4.
Hernandez-Pajares, M., & Floris, J. (1994). Classification of the hipparcos input catalogue using the kohonen network. *Monthly Notices of the Royal Astronomical Society*, *268*(2), 444–450.
Hernández-Pajares, M., Juan, J., & Sanz, J. (1997). Neural network modeling of the ionospheric electron content at global scale using GPS data. *Radio Science*, *32*(3), 1081–1089.
Hernández-Pajares, M., Juan, J., & Sanz, J. (1999). New approaches in global ionospheric determination using ground GPS data. *Journal of Atmospheric and Solar-Terrestrial Physics*, *61*(16), 1237–1247.
Hernández-Pajares, M., Juan, J., Sanz, J., Orus, R., García-Rigo, A., Feltens, J., ... Krankowski, A. (2009). The IGS VTEC maps: a reliable source of ionospheric information since 1998. *Journal of Geodesy*, *83*(3-4), 263–275.
Hernández-Pajares, M., Juan, J. M., Sanz, J., Aragón-Àngel, À., García-Rigo, A., Salazar, D., & Escudero, M. (2011). The ionosphere: effects, GPS modeling and the benefits for space geodetic techniques. *Journal of Geodesy*, *85*(12), 887–907.
Hernández-Pajares, M., et al. (2010). Section 9.4 Ionospheric model for radio techniques of Chapter 9 Models for atmospheric propagation delays of IERS Conventions 2010. *IERS Technical Note*(36).
Hernández-Pajares, M., Roma-Dollase, D., Krankowski, A., García-Rigo, A., & Orús-Pérez, R. (2017). Methodology and consistency of slant and vertical assessments for ionospheric electron content models. *Journal of Geodesy*(doi:10.1007/s00190-017-1032-z), 1-10.
Kohonen, T. (1990). The self-organizing map. *Proceedings of the IEEE*, *78*(9), 1464–1480.
Kohonen, T. (2012). *Self-organization and associative memory* (Vol. 8). Springer Science & Business Media.
Linde, Y., Buzo, A., & Gray, R. (1980). An algorithm for vector quantizer design. *IEEE Transactions on communications*, *28*(1), 84–95.
Liu, J., Chen, R., An, J., Wang, Z., & Hyyppa, J. (2014). Spherical cap harmonic analysis of the arctic ionospheric tec for one solar cycle. *Journal of Geophysical Research: Space Physics*, *119*(1), 601–619.
Liu, J., Wang, W., Burns, A., Liu, L., & McInerney, J. (2017). A tiegcm numerical study of the source and evolution of ionospheric f-region tongues of ionization: Universal time and interplanetary magnetic field dependence. *Journal of Atmospheric and Solar-Terrestrial Physics*, *156*, 87–96.
Lyu, H., Hernández-Pajares, M., Nohutcu, M., García-Rigo, A., Zhang, H., & Liu, J. (2018). The barcelona ionospheric mapping function (bimf) and its application to northern mid-latitudes. *Gps solutions*, *22*, 1–13.
Murtagh, F., & Hernández-Pajares, M. (1995). The kohonen self-organizing map method: an assessment. *Journal of Classification*, *12*(2), 165–190.
Noja, M., Stolle, C., Park, J., & Lühr, H. (2013). Longterm analysis of ionospheric polar patches based on champ tec data. *Radio Science*, *48*(3), 289–301.
Orús, R., Hernández-Pajares, M., Juan, J., & Sanz, J. (2005). Improvement of global ionospheric VTEC maps by using kriging interpolation technique. *Journal of*

Atmospheric and Solar-Terrestrial Physics, *67*(16), 1598–1609.
Robbins, H., & Monro, S. (1951). A stochastic approximation method. *The annals of mathematical statistics*, 400–407.
Roma-Dollase, D., Hernández-Pajares, M., , Krankowski, A., Ghoddousi-Fard, R., Yuan, Y., ... Gómez-Cama, J. M. (2017). Comparing vertical and slant performances of seven different global VTEC ionospheric models. *Journal of Geodesy*, *https://doi.org/10.1007/s00190-017-1088-9*.
Sojka, J. J., Bowline, M., & Schunk, R. W. (1994). Patches in the polar ionosphere: Ut and seasonal dependence. *Journal of Geophysical Research: Space Physics*, *99*(A8), 14959–14970.
Sojka, J. J., Bowline, M. D., Schunk, R. W., Decker, D. T., Valladares, C. E., Sheehan, R., ... Heelis, R. A. (1993). Modeling polar cap fregion patches using time varying convection. *Geophysical Research Letters*, *20*(17), 1783–1786.
Spicher, A., Clausen, L. B. N., Miloch, W. J., Lofstad, V., Jin, Y., & Moen, J. I. (2017). Interhemispheric study of polar cap patch occurrence based on swarm in situ data. *Journal of Geophysical Research: Space Physics*, *122*(3), 3837–3851.
Wild, J. A., Cowley, S. W. H., Davies, J. A., Khan, H., Lester, M., Milan, S. E., ... Fornacon, K. H. (2001). First simultaneous observations of flux transfer events at the high-latitude magnetopause by the cluster spacecraft and pulsed radar signatures in the conjugate ionosphere by the cutlass and eiscat radars. In *Annales geophysicae* (Vol. 19, pp. 1491–1508).
Wild, J. A., Milan, S. E., Cowley, S. W. H., Dunlop, M. W., Owen, C. J., Bosqued, J. M., ... Yukimatu, A. S. (2003). Coordinated interhemispheric superdarn radar observations of the ionospheric response to flux transfer events observed by the cluster spacecraft at the high-latitude magnetopause. In *Annales geophysicae* (Vol. 21, pp. 1807–1826).

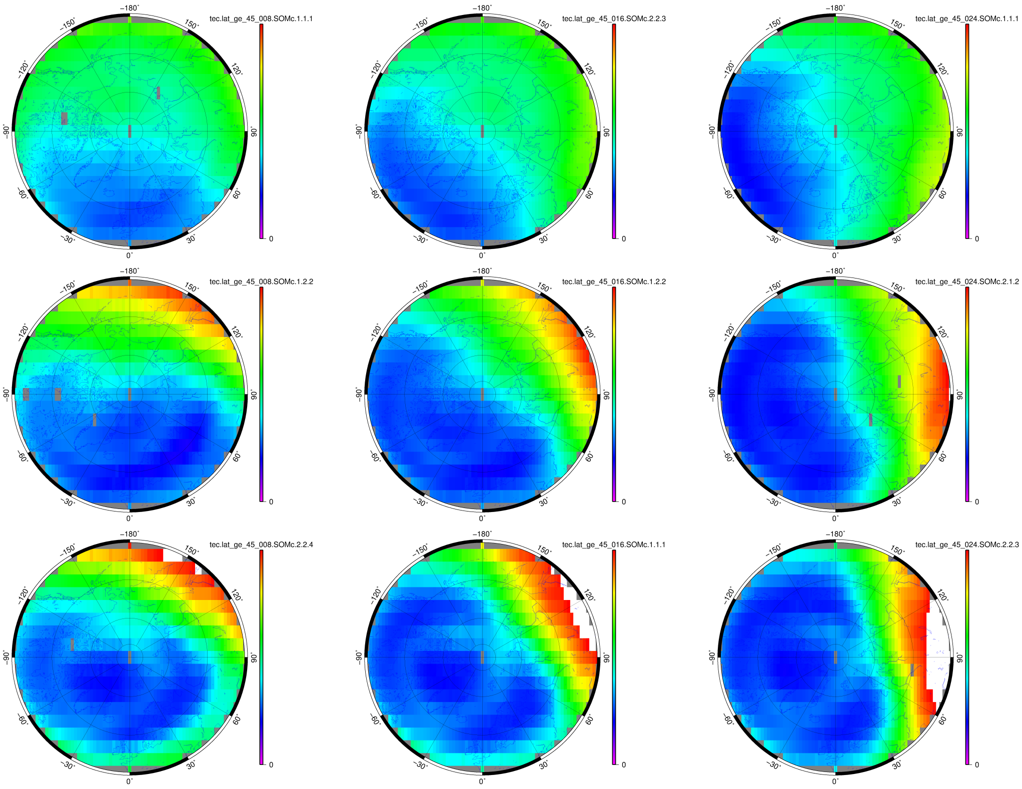

Figure A1. Centroids of normalized NPC VTEC maps (latitudes $\phi \geq 45$ deg) in the SOMs computed with 2x2 Kohonen neural network from UQRG VTEC GIMs from 2001 to the beginning of 2019 for 01.75UT (first column), 03.75UT (second column) and 05.75UT (third column).

Appendix A Detailed results of the polar GIMs clustering

A1 North Polar Ionosphere

A2 South Polar Ionosphere

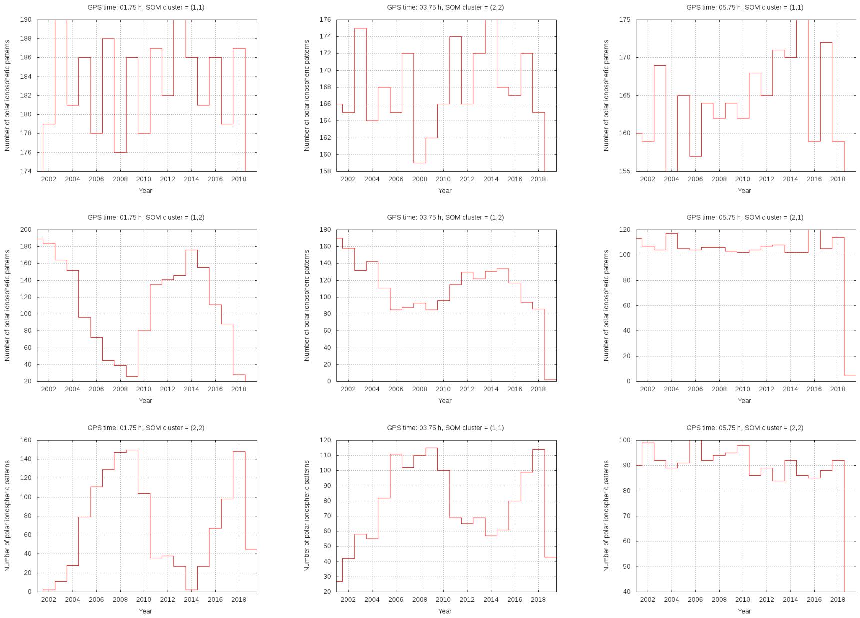

Figure A2. Occurrence per year of the individual NPC VTEC maps associated to every centroid of normalized NPC VTEC maps of Figure A1, indicated in the same order, for 01.75UT (first column), 03.75UT (second column) and 05.75UT (third column).

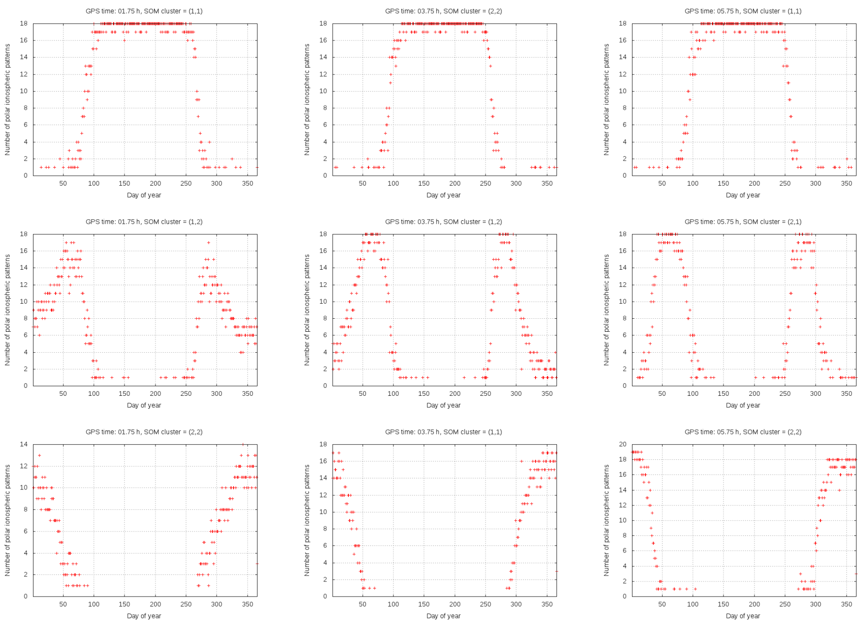

Figure A3. Occurrence per day of year of the individual NPC VTEC maps associated to every centroid of normalized NPC VTEC maps of Figure A1, indicated in the same order, for 01.75UT (first column), 03.75UT (second column) and 05.75UT (third column).

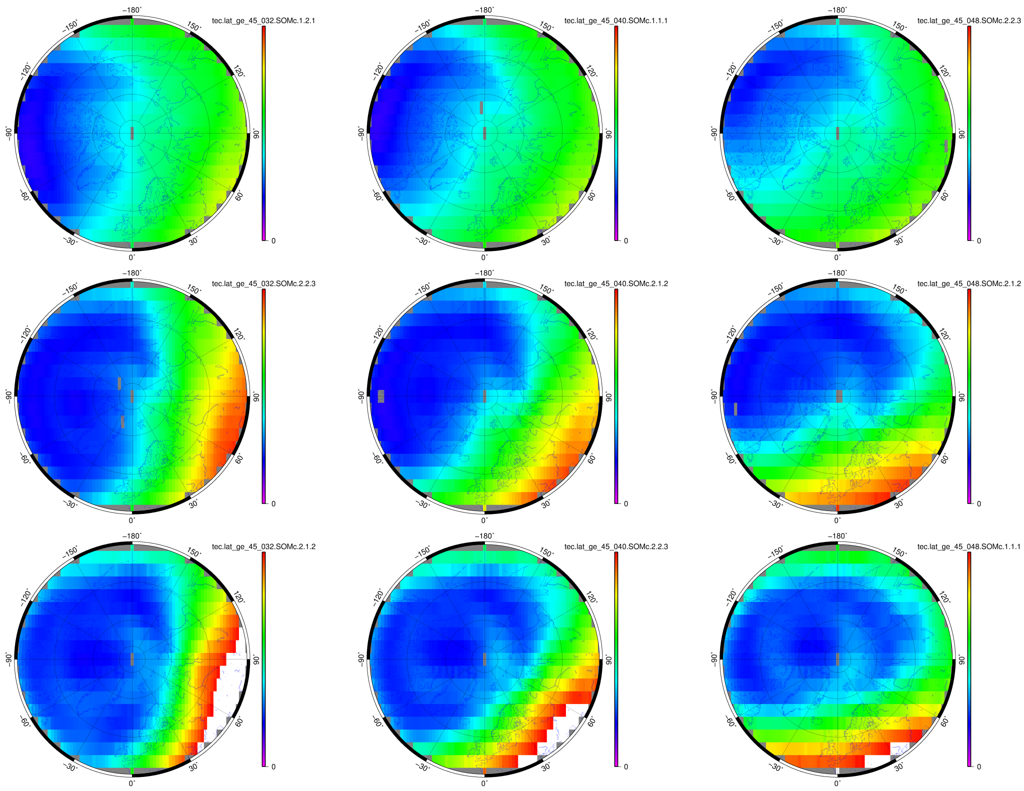

Figure A4. Centroids of normalized NPC VTEC maps (latitudes $\phi \geq 45$ deg) in the SOMs computed with 2x2 Kohonen neural network from UQRG VTEC GIMs from 2001 to the beginning of 2019 for 07.75UT (first column), 09.75UT (second column) and 11.75UT (third column).

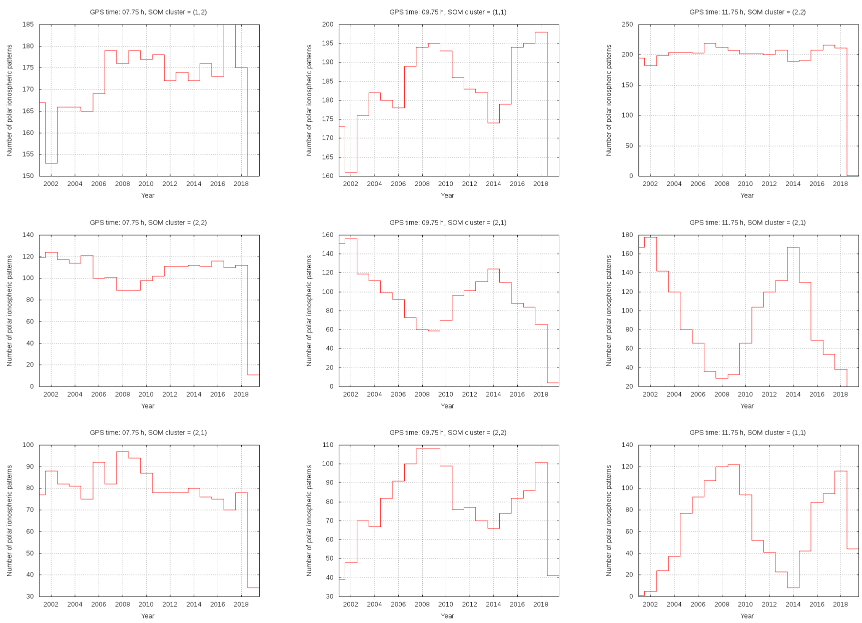

Figure A5. Occurrence per year of the individual NPC VTEC maps associated to every centroid of normalized NPC VTEC maps of Figure A4, indicated in the same order, for 07.75UT (first column), 09.75UT (second column) and 11.75UT (third column).

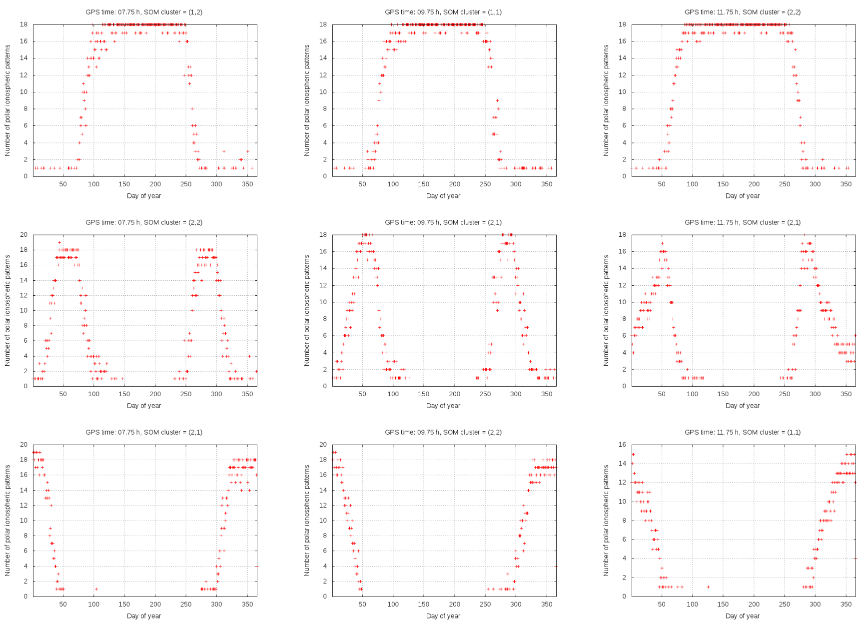

Figure A6. Occurrence per day of year of the individual NPC VTEC maps associated to every centroid of normalized NPC VTEC maps of Figure A4, indicated in the same order, for 07.75UT (first column), 09.75UT (second column) and 11.75UT (third column).

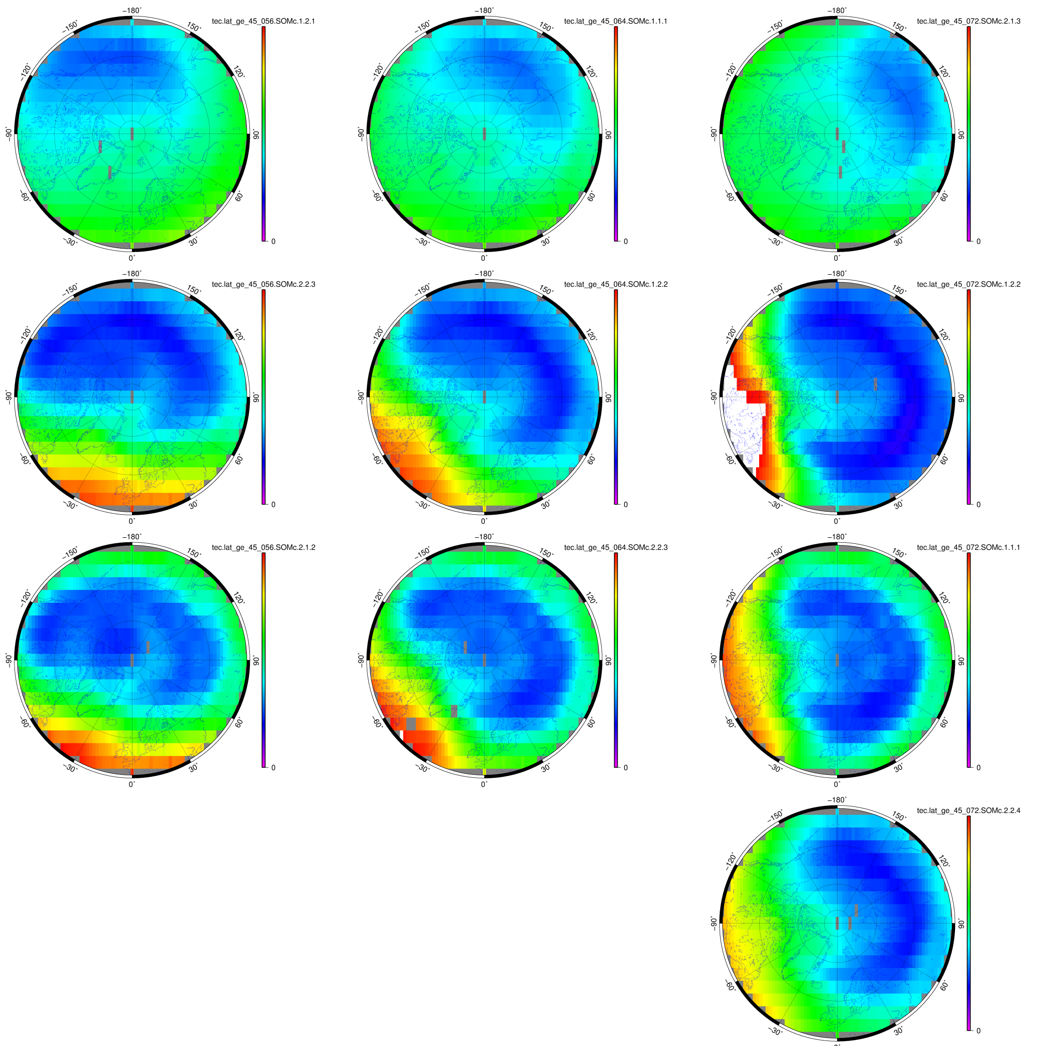

Figure A7. Centroids of normalized NPC VTEC maps (latitudes $\phi \geq 45$ deg) in the SOMs computed with 2x2 Kohonen neural network from UQRG VTEC GIMs from 2001 to the beginning of 2019 for 13.75UT (first column), 15.75UT (second column) and 17.75UT (third column).

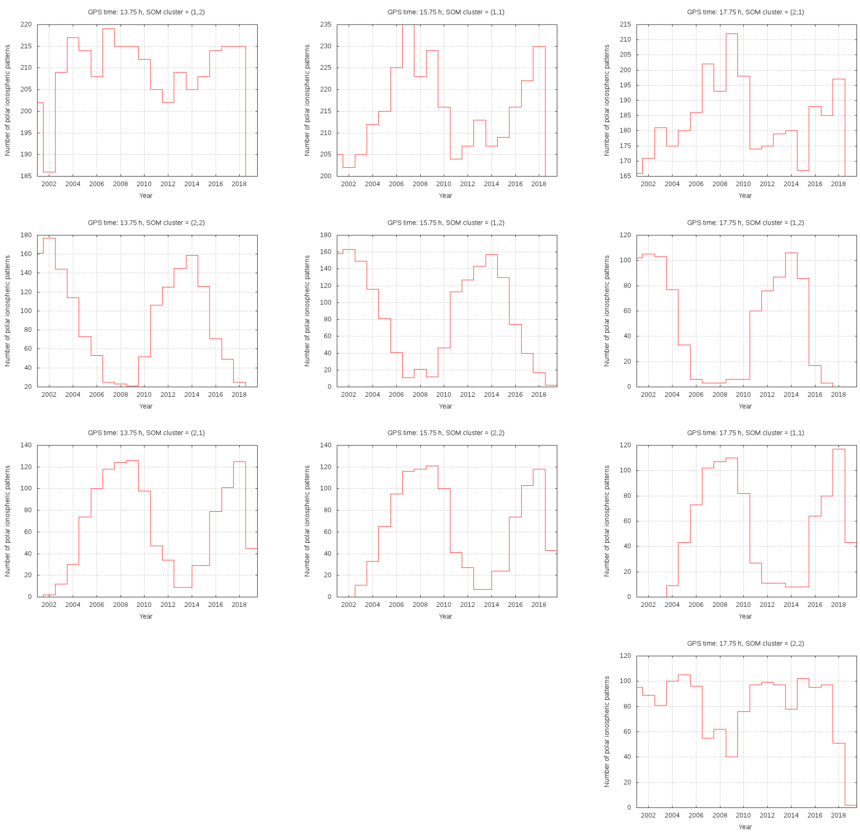

Figure A8. Occurrence per year of the individual NPC VTEC maps associated to every centroid of normalized NPC VTEC maps of Figure A7, indicated in the same order, for 13.75UT (first column), 15.75UT (second column) and 17.75UT (third column).

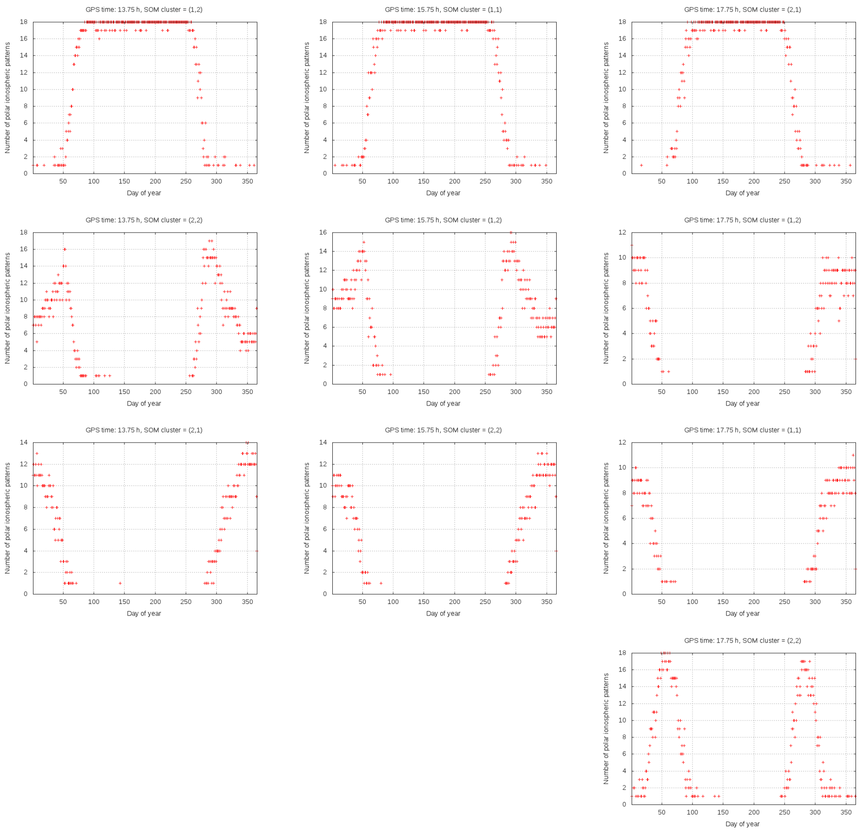

Figure A9. Occurrence per day of year of the individual NPC VTEC maps associated to every centroid of normalized NPC VTEC maps of Figure A7, indicated in the same order, for 13.75UT (first column), 15.75UT (second column) and 17.75UT (third column).

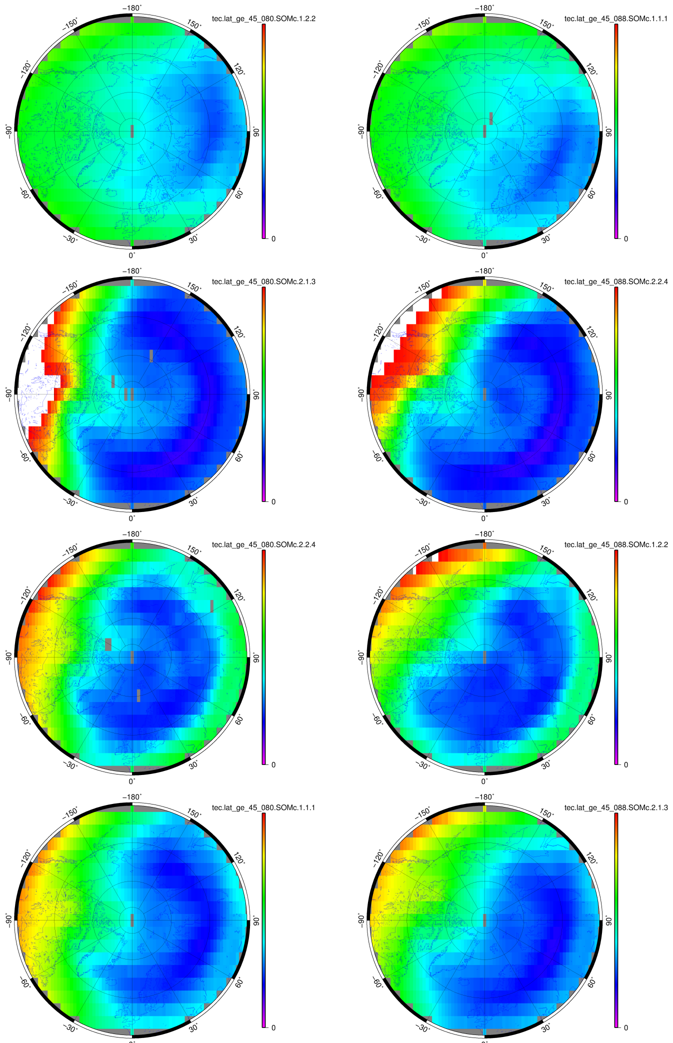

Figure A10. Centroids of normalized NPC VTEC maps (latitudes $\phi \geq 45$ deg) in the SOMs computed with 2x2 Kohonen neural network from UQRG VTEC GIMs from 2001 to the beginning of 2019 for 19.75UT (first column), 21.75UT (second column) and 23.75UT (third column).

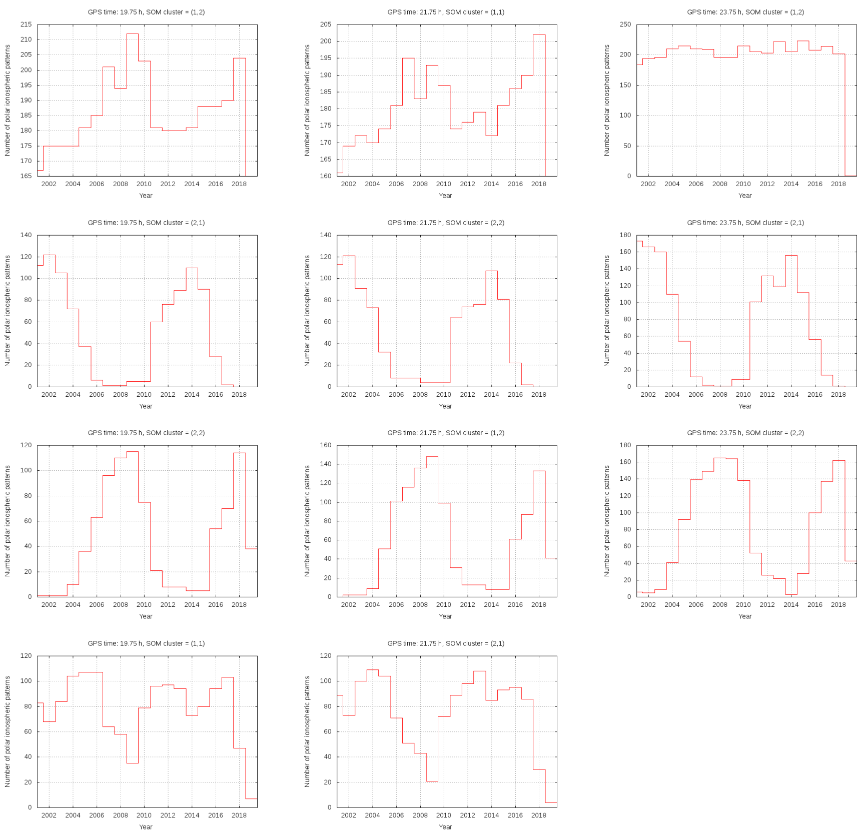

Figure A11. Occurrence per year of the individual NPC VTEC maps associated to every centroid of normalized NPC VTEC maps of Figure A10, indicated in the same order, for 19.75UT (first column), 21.75UT (second column) and 23.75UT (third column).

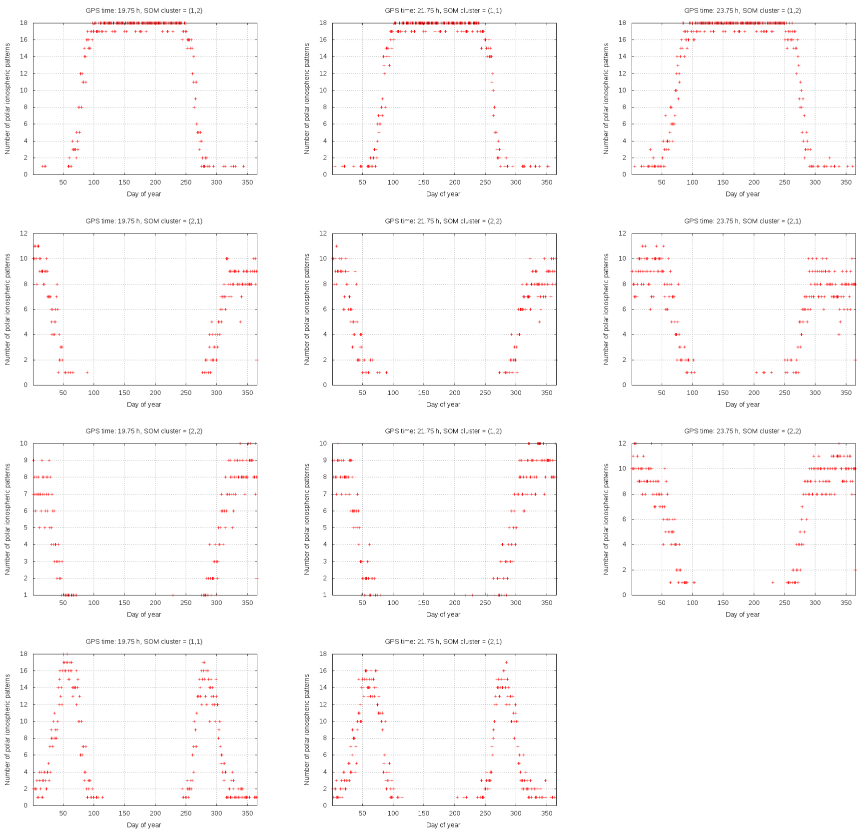

Figure A12. Occurrence per day of year of the individual NPC VTEC maps associated to every centroid of normalized NPC VTEC maps of Figure A10, indicated in the same order, for 19.75UT (first column), 21.75UT (second column) and 23.75UT (third column).

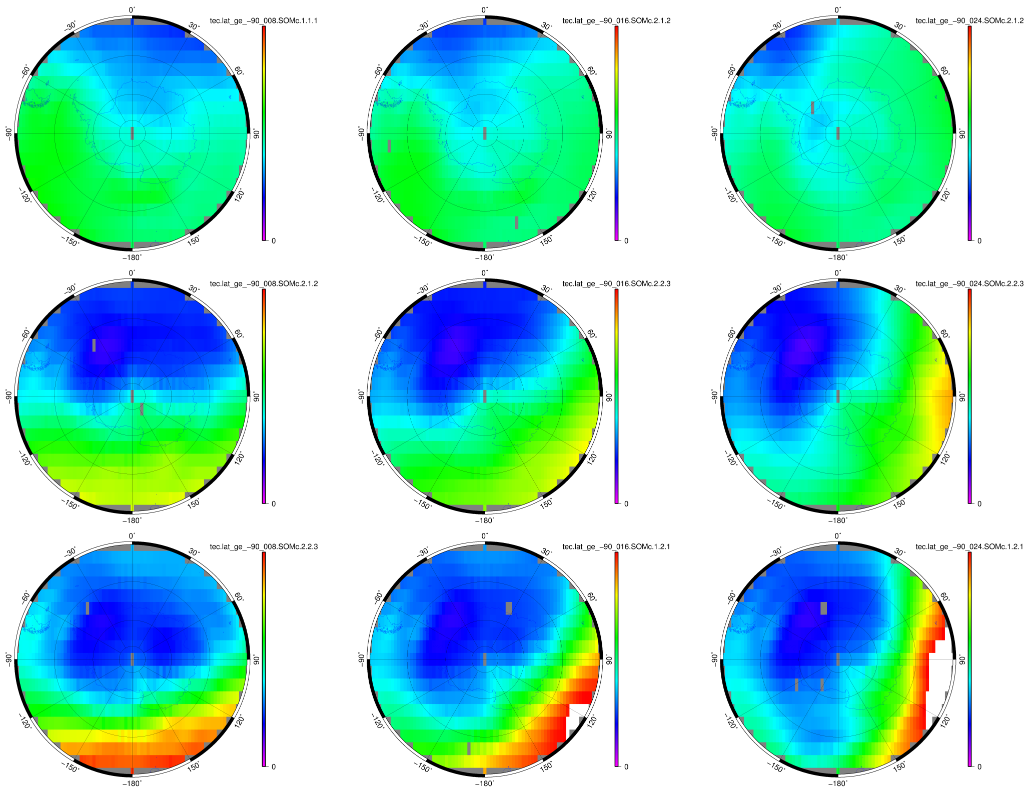

Figure A13. Centroids of normalized SPC VTEC maps (latitudes $\phi \geq 45$ deg) in the SOMs computed with 2x2 Kohonen neural network from UQRG VTEC GIMs from 2001 to the beginning of 2019 for 01.75UT (first column), 03.75UT (second column) and 05.75UT (third column).

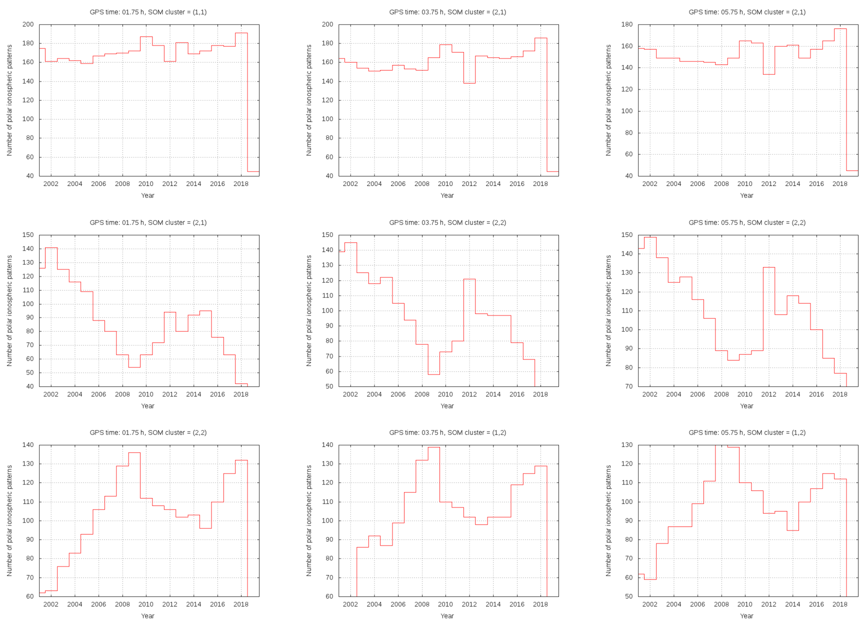

Figure A14. Occurrence per year of the individual SPC VTEC maps associated to every centroid of normalized SPC VTEC maps of Figure A13, indicated in the same order, for 01.75UT (first column), 03.75UT (second column) and 05.75UT (third column).

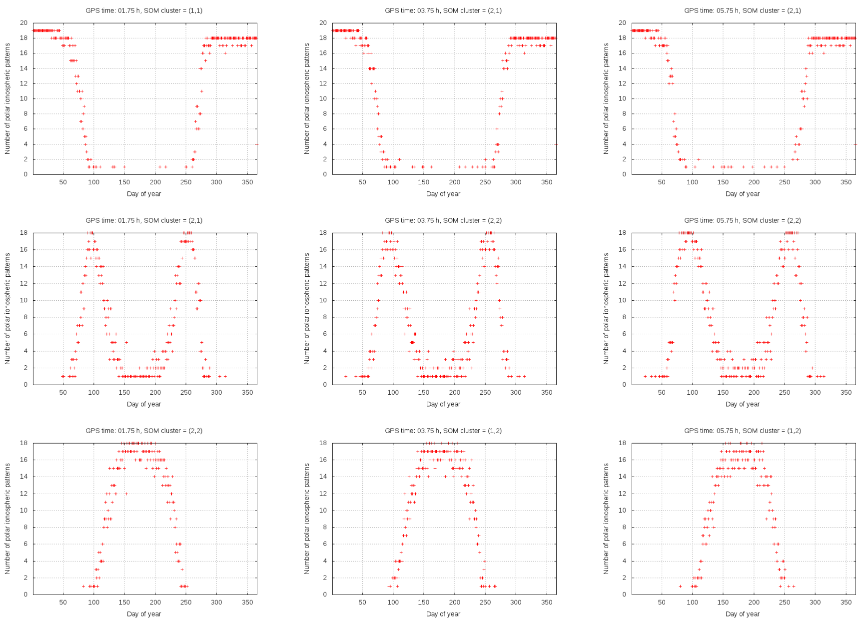

Figure A15. Occurrence per day of year of the individual SPC VTEC maps associated to every centroid of normalized SPC VTEC maps of Figure A13, indicated in the same order, for 01.75UT (first column), 03.75UT (second column) and 05.75UT (third column).

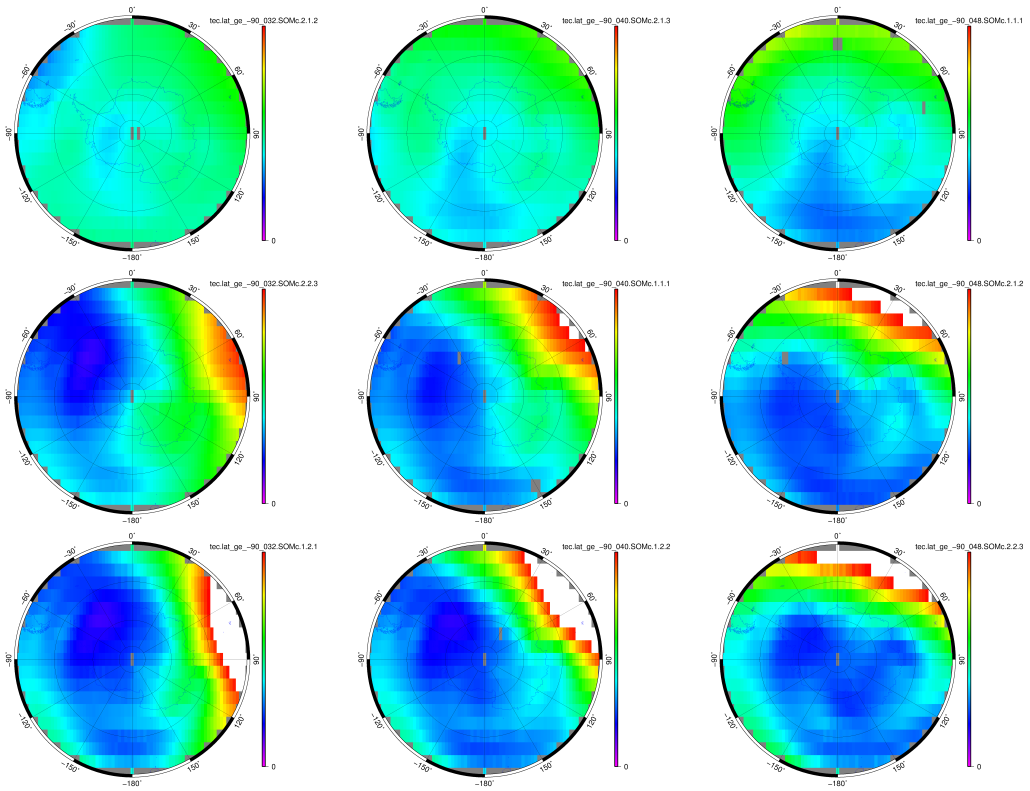

Figure A16. Centroids of normalized SPC VTEC maps (latitudes $\phi \geq 45$ deg) in the SOMs computed with 2x2 Kohonen neural network from UQRG VTEC GIMs from 2001 to the beginning of 2019 for 07.75UT (first column), 09.75UT (second column) and 11.75UT (third column).

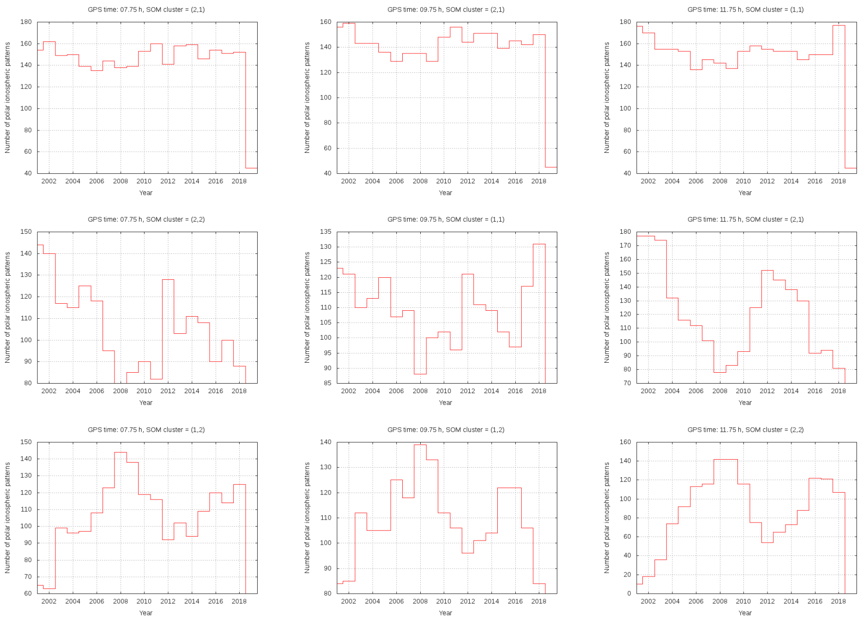

Figure A17. Occurrence per year of the individual SPC VTEC maps associated to every centroid of normalized SPC VTEC maps of Figure A16, indicated in the same order, for 07.75UT (first column), 09.75UT (second column) and 11.75UT (third column).

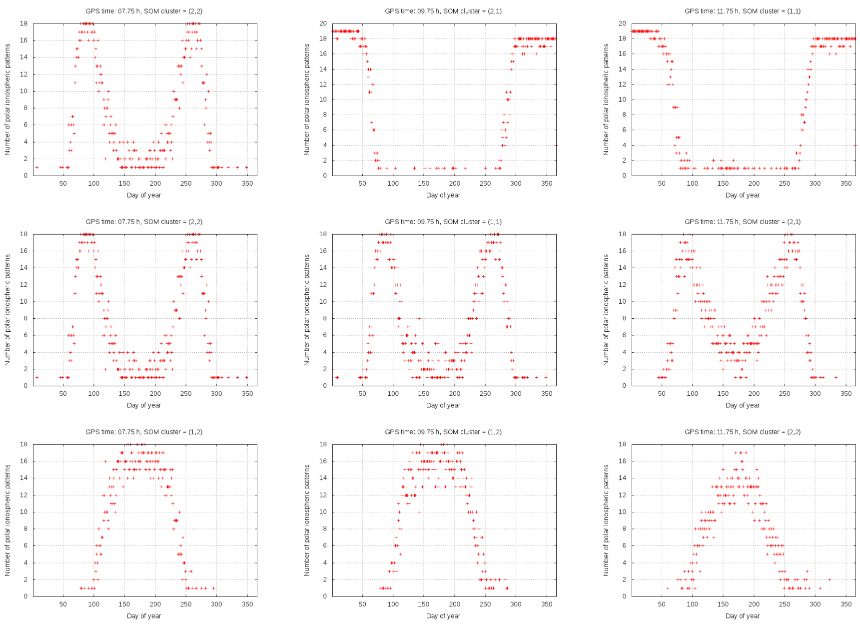

Figure A18. Occurrence per day of year of the individual SPC VTEC maps associated to every centroid of normalized SPC VTEC maps of Figure A16, indicated in the same order, for 07.75UT (first column), 09.75UT (second column) and 11.75UT (third column).

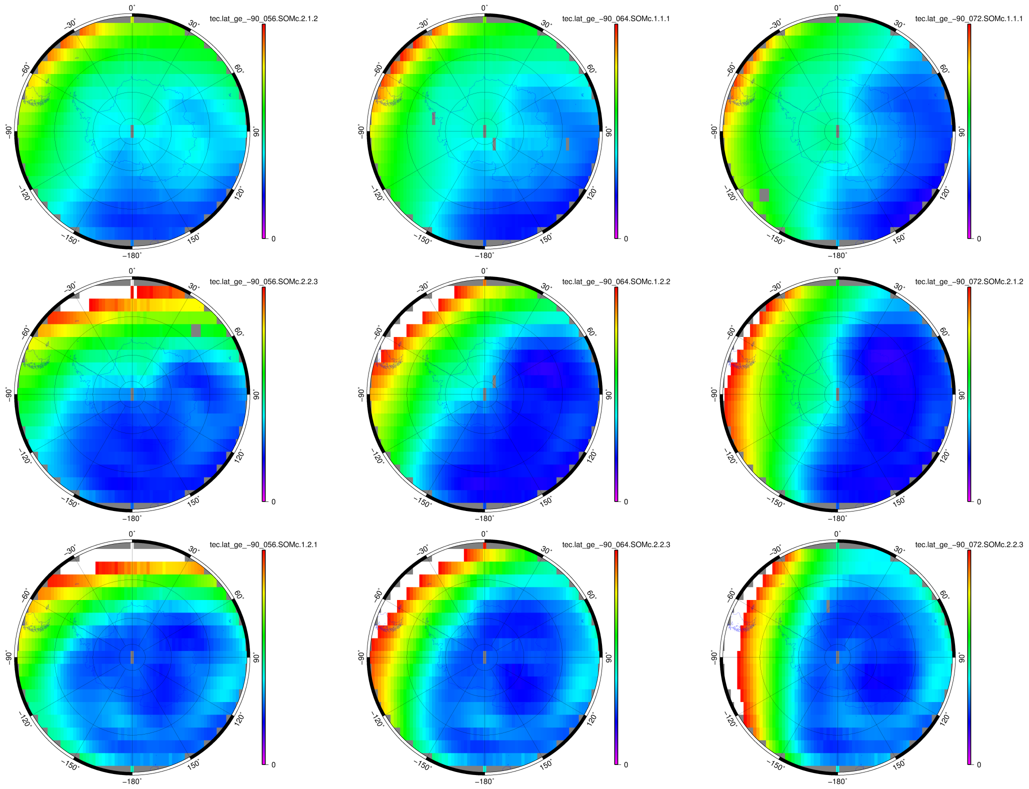

Figure A19. Centroids of normalized SPC VTEC maps (latitudes $\phi \geq 45$ deg) in the SOMs computed with 2x2 Kohonen neural network from UQRG VTEC GIMs from 2001 to the beginning of 2019 for 13.75UT (first column), 15.75UT (second column) and 17.75UT (third column).

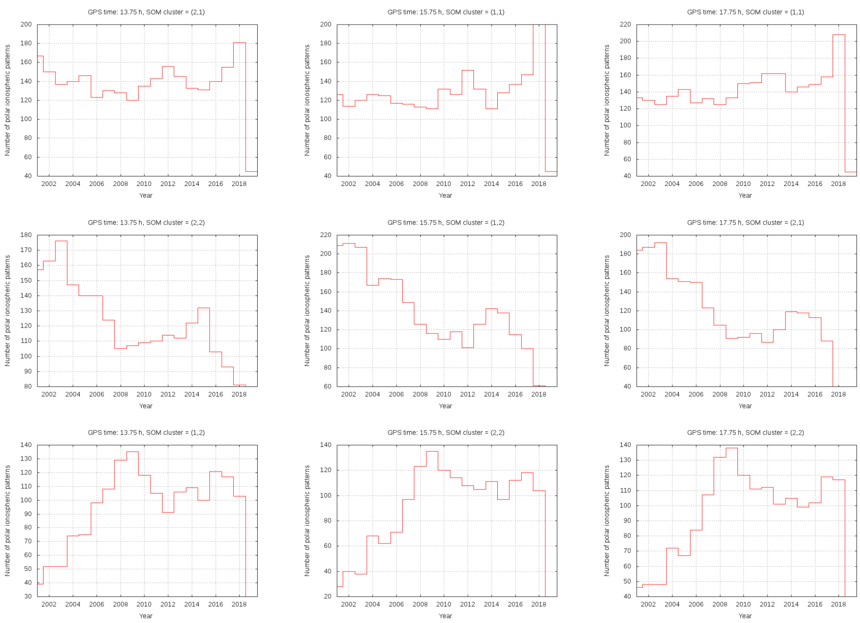

Figure A20. Occurrence per year of the individual SPC VTEC maps associated to every centroid of normalized SPC VTEC maps of Figure A19, indicated in the same order, for 13.75UT (first column), 15.75UT (second column) and 17.75UT (third column).

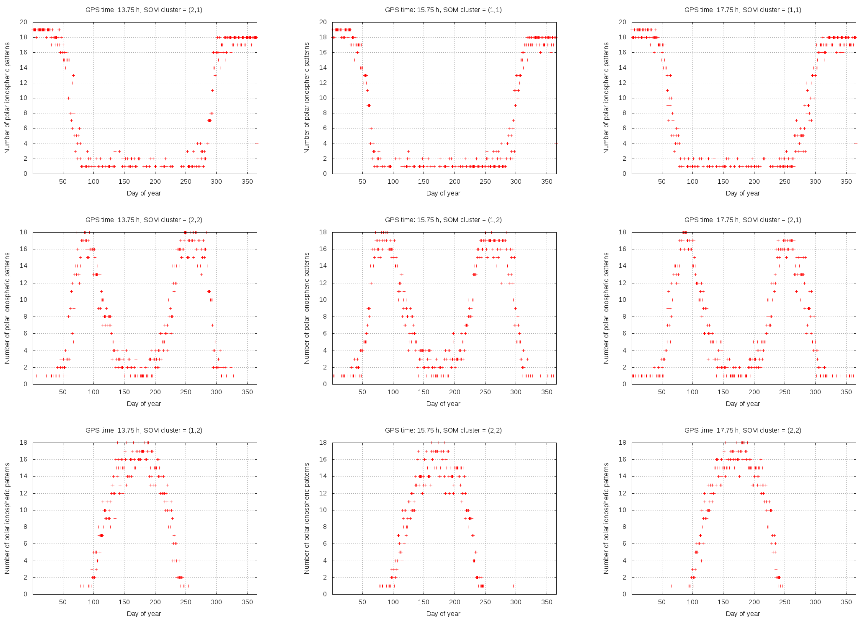

Figure A21. Occurrence per day of year of the individual SPC VTEC maps associated to every centroid of normalized SPC VTEC maps of Figure A19, indicated in the same order, for 13.75UT (first column), 15.75UT (second column) and 17.75UT (third column).

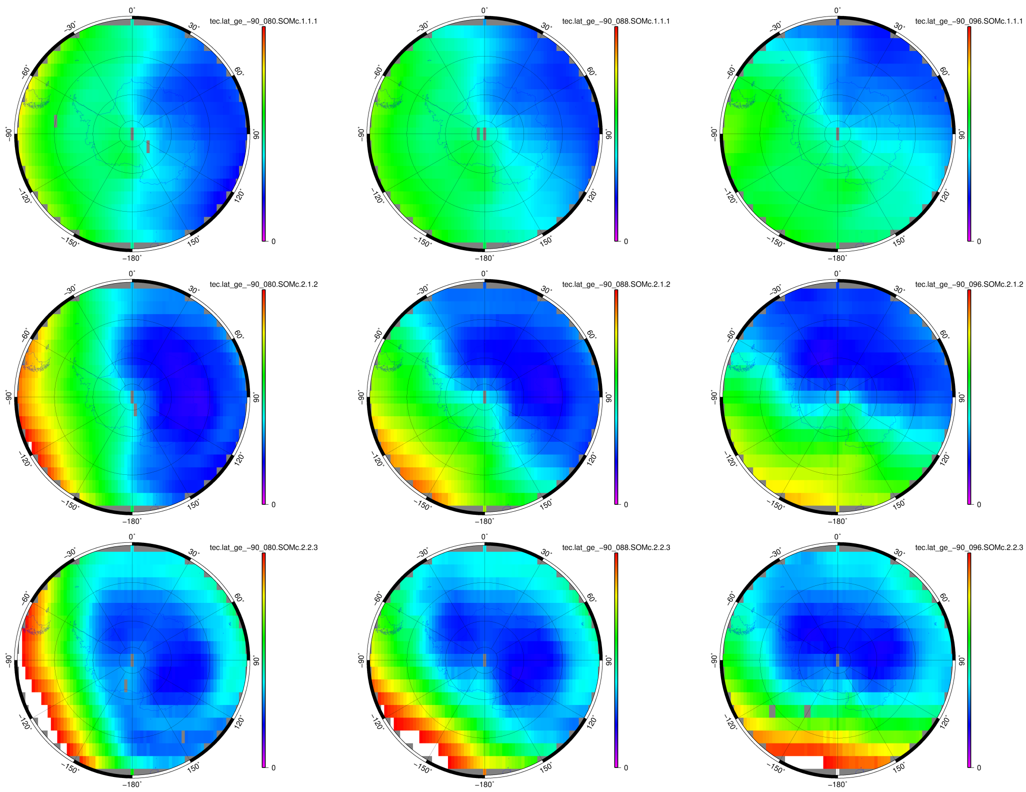

i

Figure A22. Centroids of normalized SPC VTEC maps (latitudes $\phi \geq 45$ deg) in the SOMs computed with 2x2 Kohonen neural network from UQRG VTEC GIMs from 2001 to the beginning of 2019 for 19.75UT (first column), 21.75UT (second column) and 23.75UT (third column).

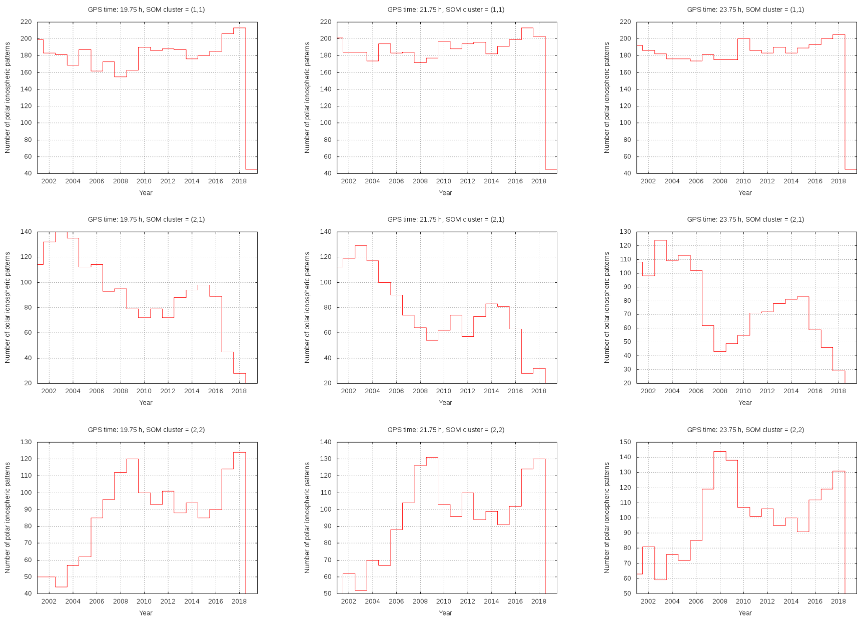

Figure A23. Occurrence per year of the individual SPC VTEC maps associated to every centroid of normalized SPC VTEC maps of Figure A22, indicated in the same order, for 19.75UT (first column), 21.75UT (second column) and 23.75UT (third column).

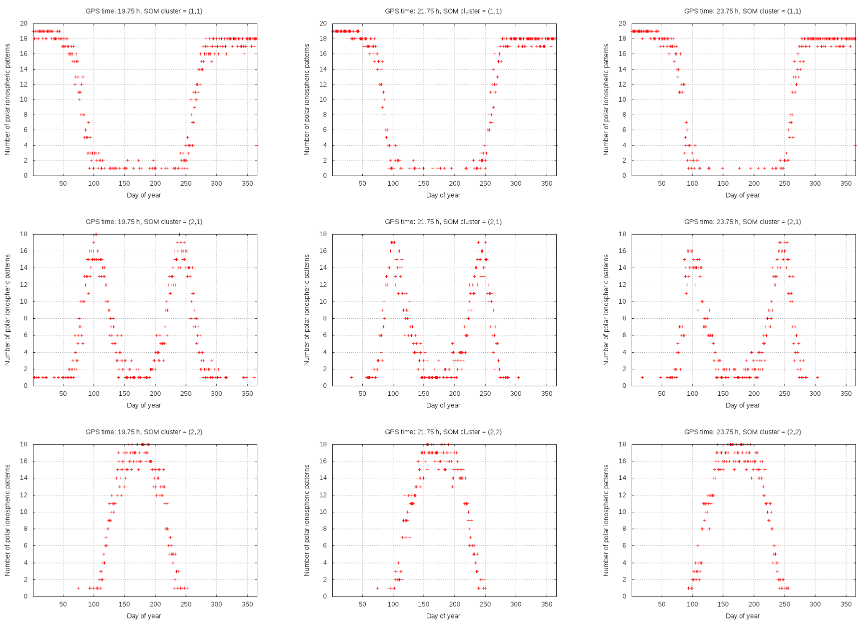

Figure A24. Occurrence per day of year of the individual SPC VTEC maps associated to every centroid of normalized SPC VTEC maps of Figure A22, indicated in the same order, for 19.75UT (first column), 21.75UT (second column) and 23.75UT (third column).